

國立台灣大學醫學院暨工學院醫學工程研究所

碩士論文

Graduate Institute of Biomedical Engineering

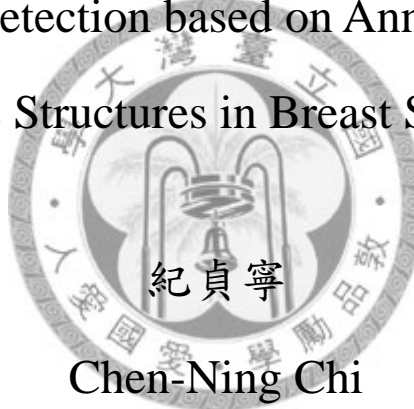
College of Medicine and College of Engineering

National Taiwan University

Master thesis

以乳房解剖學結構標註為基礎之超音波腫瘤偵測

Lesion Detection based on Annotation of
Anatomic Structures in Breast Sonograms



指導教授：陳中明 博士

Adviser : Chung-Ming Chen, PH.D.

中華民國 98 年 8 月

August, 2009

中文摘要

乳癌是女性癌症中最常出現的一種，超過 40 歲的女性得到乳癌將有極高的致死率。如能提早發現便可提早治療以減低乳癌的致死率。

現今有一些技術被用於乳癌診斷，例如：乳腺 X 光攝影檢查術 (mammography)，核磁共振造影 (magnetic resonance imaging, i.e., MRI) 與超音波技術 (sonograms, i.e., ultrasound images)。由於超音波影像技術有 3 大優點：方便性，非侵入性與較低成本花費。所以超音波影像技術已成為現今罹患乳癌高危險女性群的主要乳癌掃描方法之一。超音波乳癌掃描技術在乳癌診斷占了很重要的地位。

超音波乳癌掃描技術目前已經從傳統二維影像技術發展為三維體積資料影像技術，而一份三維體積資料影像是由數百張二維影像所建構出來的。發展電腦輔助偵測系統(computer-aided detection, CAD)來自動偵測乳癌於一連串二維乳房超音波影像的技術，將會幫助醫生與放射師的病理診斷，並且對於乳癌掃描技術有莫大的幫助。

雖然目前已有不少電腦輔助偵測乳癌的研究發表，但是因為超音波影像本身既有的超音波假影問題，增加了偵測結果的錯誤率。一個可減少錯誤率的方法是從乳房解剖學上的資訊來做分析。就解剖學而言，大部分腫瘤發生的位置是位在脂肪層與肌肉層中間的乳房組織。

在這篇文章中，我們將提出一個新的偵測演算法，首先會先偵測超音波影像中的脂肪層與肌肉層，接著再對兩層之間的區域即乳房組織做乳癌偵測的動作。肌肉層偵測的概念主要是去確認影像中有豐富水平資訊的區域，這些區域可藉由賈柏濾波器 (Gabor filters) 和相位對稱性 (phase symmetry) 的計算得到。接著利用自動選定臨界值技術 (automatic thresholding selection) 和拓樸學關係性 (topological relation) 去偵測影像中脂肪層的區域。一旦影像中的脂肪層與肌肉層皆被確認出，接著偵測彼此兩層所夾的中間區域裡的具高機率為腫瘤的可疑組織。

利用乳房解剖學資訊的分析將可以提高乳癌偵測的準確率。最後本論文藉由

60 張超音波影像來進行準確率計算。由結果可以知道，大多數的囊腫（cysts）與腫瘤（lesions）皆可以很成功地被偵測出，證明本論文所發展的演算法具有高的準確率。

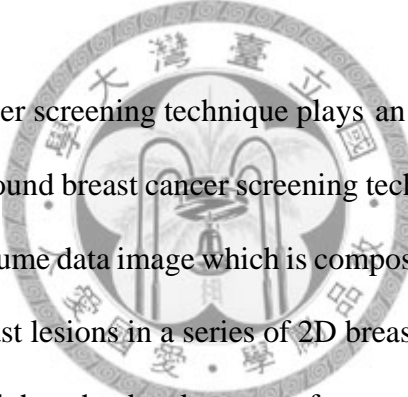
關鍵詞：乳房超音波、電腦輔助偵測、乳房解剖學資訊、肌肉層偵測、脂肪層偵測、自動化腫瘤偵測



Abstract

Breast cancer is one of the most frequent types of cancer found in females, and it has the highest incident rate of all cancers among females over the age of 40. Therefore, it is important to detect and treat it at an early stage.

There are several breast cancer diagnosis techniques, like mammography, magnetic resonance imaging (MRI), sonograms (ultrasound images), etc. With the benefits of ultrasound, convenience, non-invasiveness and relatively low cost, ultrasound images are considered as useful information on the screening of females at high risk for breast cancer.



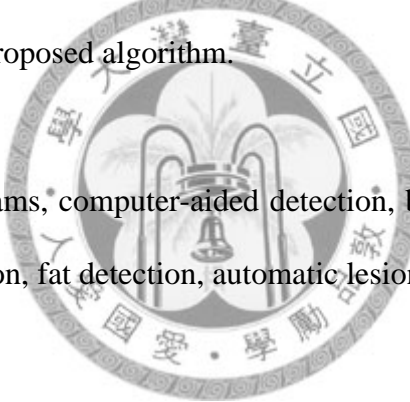
Ultrasound breast cancer screening technique plays an important role in the field of the breast diagnosis. Ultrasound breast cancer screening technique has progressed from a 2D single image to a 3D volume data image which is composed of hundreds of 2D images. Automatic detection of breast lesions in a series of 2D breast sonograms is great help for breast cancer screening; and thus the development of computer-aided detection (CAD) is needed. It provides a convenient way for doctors and radiologists to detect breast cancer while using ultrasound images. A lot of methods for computer-aided detection systems using ultrasound images have been developed by many researchers around the world.

While several approaches have been proposed previously, the false positive rate still tends to be too high for practical use because of the sonographic artifacts. One possible way to reduce the false positive rate is to incorporate the anatomic information into the decision-making strategy. For anatomic information, most lesions appearing in breast tissue are located in-between the fat layer and the muscle layer in sonograms

In this thesis, we present a new detection algorithm for identification of the fat and

muscle layers first, and use the in-between region of those two layers to detect lesions. For muscle layer detection, the basic idea is to identify the area with rich horizontal strip texture patterns by a newly developed texture descriptor computed by the Gabor filters and phase symmetry techniques. For fat layer detection, an automatic thresholding approach in collaboration with a topological relation is proposed. Once the fat and muscle layers are determined, the hypoechoic regions in-between these two layers are more likely to be a breast lesion.

Analysis of anatomic information of breast may increase the accuracy of lesion detection in a single breast ultrasound image. Having examining 60 ultrasound test cases, almost all the cysts and lesions could be detected successfully. The experimental results prove the accuracy of the proposed algorithm.



Key words: Breast sonograms, computer-aided detection, breast anatomic information, muscle detection, fat detection, automatic lesion detection

Contents

中文摘要	1
Abstract	3
Contents.....	5
List of Figures	6
List of Tables	8
1 Introduction	9
1.1 Introduction	10
1.2 Motivation	13
1.3 Organization	16
1.4 Contribution	17
1.5 Data source.....	18
2 Reference literature	19
3 Method and Material	25
3.1 Gabor Filter	28
3.2 Phase Symmetry.....	37
3.3 Entropy	43
3.4 Thresholding	48
4 Implementation and Results.....	53
5 Conclusion and Discussion	85
Ref	88

List of Figures

Fig 1.1 : The relation between 3D volume image and 2D images	11
Fig 1.2 : The artifacts appears on the muscle layer	13
Fig 1.3 : The problem of the fat layer.....	14
Fig 1.4 : The major tissues of anatomic information in breast ultrasound images	15
Fig 2.1 : The relation of the variables of skewness	21
Fig 2.2 : Two examples about Canny edge detector	22
Fig 3.1.1 : An example of two different orientations even Gabor filters	31
Fig 3.1.2 : An example of two different frequencies even Gabor filters	31
Fig 3.1.3 : A rosette map.....	32
Fig 3.1.4 : Comparison between the even and odd Gabor filters	34
Fig 3.2.1-Fig3.2.3 : An artificial image deals with the even and odd Gabor filters	
Fig 3.2.1 : An artificial image information.....	38
Fig 3.2.2 : (a),(c) : The even Gabor filter information	
(b),(d) : The odd Gabor filter information	38
Fig 3.2.3 : (a),(c),(e) : The results by using the even Gabor filter	
(b),(d),(f) : The results by using the odd Gabor filter	39
Fig 3.2.4 : An example about PS map of the ultrasound image	42
Fig 3.3.1 : Examples about interpretation of weighting angle distribution of patterns	
(a)(c)(e) : the image example about entropy value is larger	
(b)(d)(f) : the image example about entropy value is smaller	46
Fig 3.4.1 : An example about estimating optimal threshold selection	
(a) : original image	
(b) : the better threshold example	
(c) : the worse threshold example	51
Fig 4.1 : The flow char of this article	54
Fig 4.2 : The cyst case 1 : a cyst	60
Fig 4.3 : The benign lesion case 1 : a simple benign lesion	61
Fig 4.4 : The benign lesion case 2 : a benign lesion	62
Fig 4.5 : The benign lesion case 3 : a benign lesion	63
Fig 4.6 : The benign lesion case 4 : a benign lesion	64
Fig 4.7 : The benign lesion case 5 : a benign lesion	65
Fig 4.8 : The benign lesion case 6 : a benign lesion (with artifact).....	66
Fig 4.9 : The malignant lesion case 1 : a simple malignant lesion	67
Fig 4.10 : The malignant lesion case 2 : a simple malignant lesion	68
Fig 4.11 : The malignant lesion case 3 : a malignant lesion	69

Fig 4.12 : The malignant lesion case 4 : a malignant lesion.....	70
Fig 4.13 : The malignant lesion case 5 : a malignant lesion.....	71
Fig 4.14 : The malignant lesion case 6 : a malignant lesion(with artifact).....	72
Fig 4.15 : The malignant lesion case 7 : a malignant lesion(with artifact).....	73
Fig 4.16 : The malignant lesion case 8 : a malignant lesion(with artifact).....	74
Fig 4.17 : The malignant lesion case 9 : a malignant lesion(with artifact).....	75
Fig 4.18 : The malignant lesion case 10 : a malignant lesion(with artifact).....	76
Fig 4.19 : The malignant lesion case 11 : a malignant lesion(with artifact).....	77
Fig 4.20 : The malignant lesion case 12 : a malignant lesion(with artifact).....	78
Fig 4.21 : The malignant lesion case 13 : a malignant lesion(with artifact).....	79
Fig 4.22 : The unsuccessful case 1 : a benign lesion	80
Fig 4.23 : The unsuccessful case 2 : a benign lesion	81
Fig 4.24 : The unsuccessful case 3 : a benign lesion	82
Fig 4.25 : The unsuccessful case 4 : a malignant lesion	83



List of Tables

Table.1 Accuracy of lesion detection estimated by our approach.....84



Chapter 1

Introduction

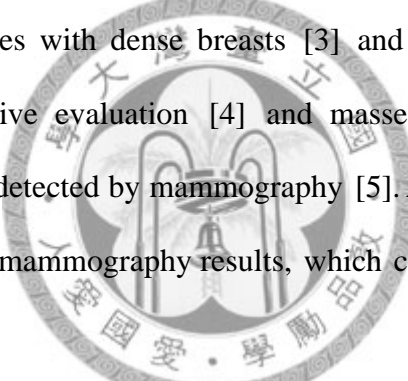
The objective of this thesis is to develop and implement an automatic lesion detection approach for breast ultrasound images. In this chapter, a brief introduction of breast cancer, ultrasound image techniques, and computer-aided detection (CAD) systems are present, the research motivation is described, and the organization of the thesis is given. Finally, a summary about contribution of this thesis is made.



1.1 Introduction

Breast cancer is a leading cause of death prevalent among females in developed countries. Detection of breast cancer at an early stage may increase success of treatment, and it is recommended generally that screening for breast cancer in females over 40 [1]. Currently, it would be a standard method that combines sonography (i.e., ultrasound image) or magnetic resonance imaging (MRI) [2] to detect and diagnose breast cancer with mammography, which is used for periodic screening of females over 40 years old.,

The qualities of ultrasound images as an adjunct to mammography in screening have been studied over the last two decades. Ultrasound is especially helpful to detect occult malignancies among females with dense breasts [3] and particularly consider breast conservation for preoperative evaluation [4] and masses detection associated with micro-calcifications likely detected by mammography [5]. A study proposed ultrasound techniques as an adjunct to mammography results, which can increase the accuracy rate of diagnoses [6].



In [7], ultrasound was presented to be more effective for females under 35 years old than mammography; because it is apt to interpret ultrasound images than mammograms of younger females. The utility of ultrasound breast screening was mentioned in [8]; 3000 female patients had dense breast examined by the ultrasound technique but shown as normal by mammographic or physical examination. These females patients used the ultrasound technique with increased 17% correctness of cancer detection overall. It means that ultrasound is capable of detecting a mass even in dense breasts. Ultrasound has been used widely for detection as well as breast mass classification. More benefits of ultrasound equipments are inexpensive, portable and not involving ionizing radiation

than other techniques. Based on the above reasons, ultrasound technique has potential to be a breast lesion screening tool.

Recently, ultrasound technique has developed from a 2D single image to a 3D volume data image and becomes more popular than ever. A 3D ultrasound volume data image is composed of a sequence of hundreds of successive 2D images as shown in Fig 1.1.

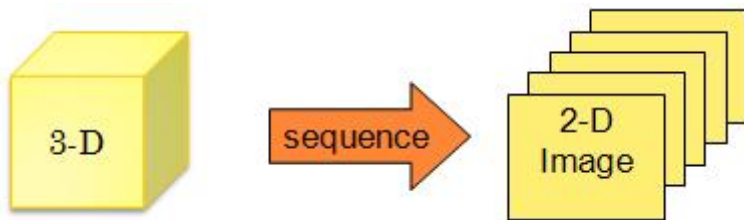
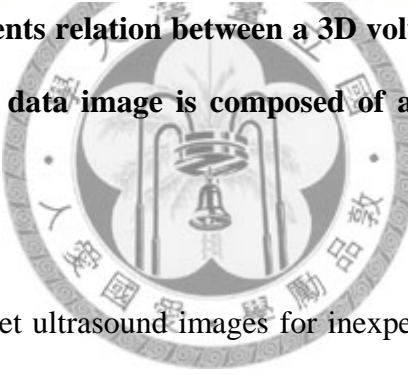


Fig 1.1 This figure presents relation between a 3D volume image and 2D images. **A 3D ultrasound volume data image is composed of a sequence of hundreds of successive 2D images.**



It is not easy to interpret ultrasound images for inexperienced radiologists because the quality of ultrasound images is poor. Therefore, the large amount of screening 2D ultrasound images can be a burden to radiologists. In addition, human observers are apt to miss small lesions in 3D volume data images. Based on the above, it is important to develop computer-aided detection (CAD) to assist clinical physicians to detect breast lesions by using ultrasound images. CAD computerizes analyses of the ultrasound images to automatically provide objectively and identifiably important information to clinical diagnoses.

CAD is a useful tool in the research of medical images. Physicians use computers as the second radiologist to determine abnormal breast tissues. Nevertheless, previous

automatic breast screening techniques have defects which are similar to identify a region of interest (ROI) of the lesions by providing information manually [9][10]. Several breast lesion segmentation approaches could merely work on ultrasound images which already known with lesions [11]. However, an actual CAD system should detect the ROI of lesions automatically and use the ROI to segment lesions. While dealing with breast ultrasound images, those are the potential problems of CAD systems.

It is difficult to automatically detect lesions in ultrasound images due to the variance in shape based on the type of lesions, the low contrast between objects and backgrounds, and ultrasound potential artifacts, like speckle noise interference. Recently, there are several approaches of CAD, which are explored by various researchers in breast ultrasound images [11] - [15].



1.2 Motivation

Although several approaches have been proposed previously, the false positive rate tends to be too high for practical uses because of the sonographic artifacts, one of potential problems in sonograms. Most artifacts shown on a muscle layer are resulted in the shadowing effect, and may be mistaken as lesions. An example is shown in Fig 1.2. The problem on a fat layer is that both fat and lesions are dark regions. It's indistinguishable in some lesion detection algorithm. An example is shown in Fig 1.3.



Fig 1.2 This figure presents artifacts shown on a muscle layer. An extensive shadowing posterior to a lesion is one of sonographic artifacts, which makes lesion detection more difficult. These shadowed regions can be mistaken as additional lesions and lead to false-positive detection.

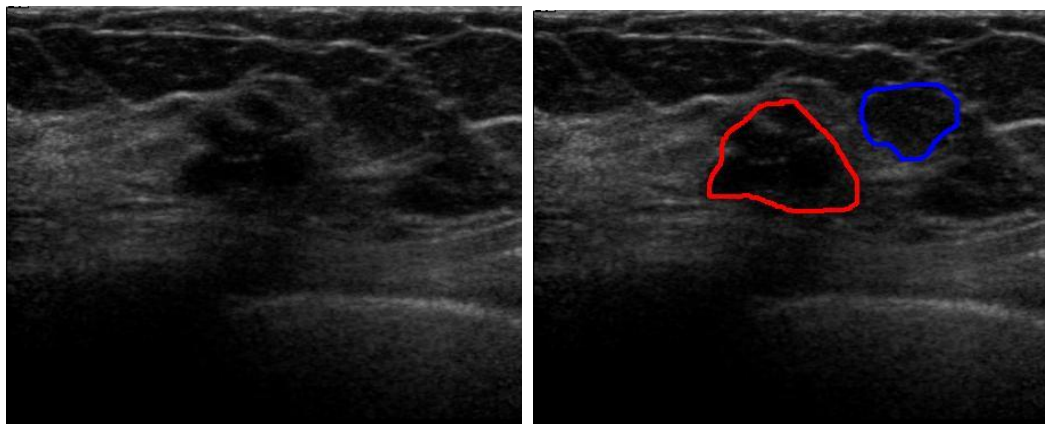
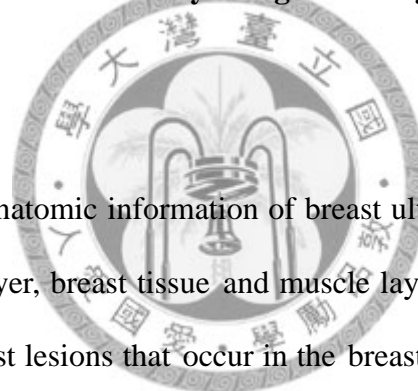


Fig 1.3 This figure presents a problem of a fat layer. The left figure is original image. The right figure points out a lesion and one part of the fat layer. The red one is the lesion, and the blue one is the part of the fat layer. In this example, the blue one may be detected as a lesion by using some edge detectors for its vertical edge.



The major tissue of anatomic information of breast ultrasound images from top to bottom includes the fat layer, breast tissue and muscle layer, as shown in Fig 1.4. For anatomic information, most lesions that occur in the breast tissue are called mammary carcinoma, the most common type of breast cancer in women. It comes in two forms: one is infiltrating carcinoma, an invasive, malignant, and abnormal proliferation of neoplastic cells in the breast tissue; the other is carcinoma in situ, a noninvasive, possibly benignant, and cysts.

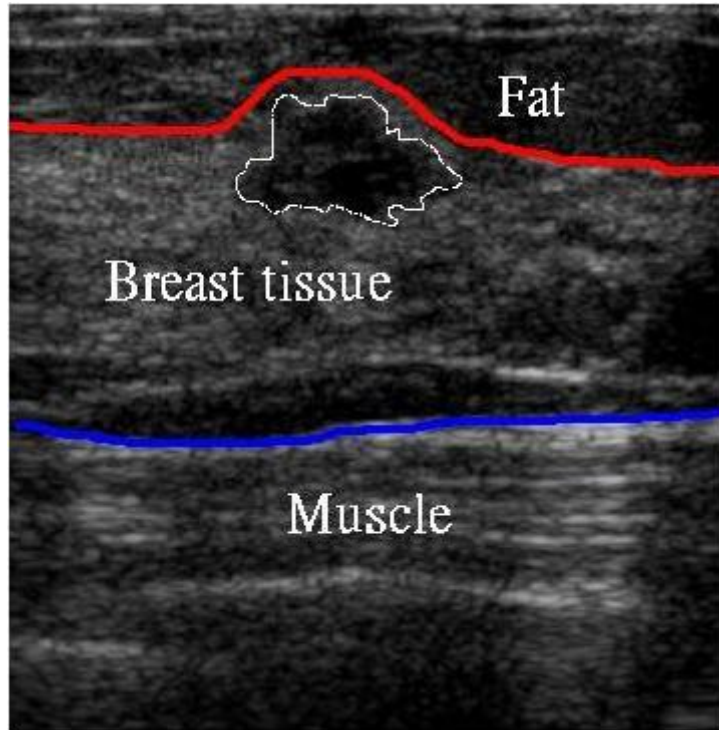
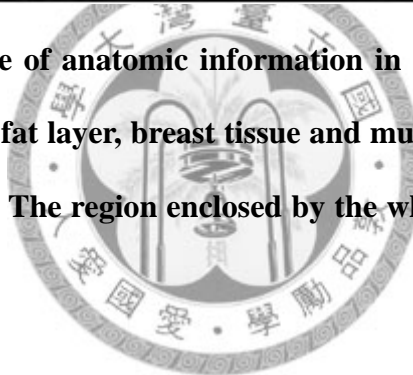


Fig 1.4 The major tissue of anatomic information in a breast ultrasound image from top to bottom is the fat layer, breast tissue and muscle layer, and most lesions occur in the breast tissue. The region enclosed by the white contour is the lesion in this example.



The basic idea of this article is to incorporate the anatomic information into the decision-making strategy. In this article, we present a new detection algorithm to identify fat and muscle layers first. Once the fat and muscle layers are determined, the hypoechoic regions in-between these two layers are more likely to be a breast lesion.

1.3 Organization

Chap.1 Introduction: This chapter briefly introduces the research background and describe the motivation and contribution.

Chap.2 Reference literatures: This chapter briefly introduces literatures with relevant topics of detection of lesions on ultrasound images [11] - [15].

Chap.3 Method and Material: The approaches used in this article are discussed, including Gabor filters, phase symmetry, entropy for detection of the muscle layer, a thresholding technique for detection of the fat layer, and lesion detection.

Chap.4 Implementation and Results: In Chapter 4, the details of implementation are mentioned and the results of muscle detection, fat detection, and lesion detection are shown, respectively.

Chap 5 Discussion and Conclusions: This chapter concludes the thesis with a summary of the main results along with some description of future research.

1.4 Contribution

Because most lesions occur in breast tissue, we use anatomic information in the decision-making strategy. The major tissue anatomic information of a breast ultrasound image from top to bottom, shown in Fig 1.4, includes the fat layer, the breast tissue and the muscle layer. In this thesis, we present a new detection algorithm for identification of fat and muscle layers first, and the preliminary results show that these two detection techniques may be served as the first step toward automatic lesion detection.

For muscle layer detection, the basic idea is to identify the area with rich horizontal strip texture patterns by a newly developed texture descriptor using Gabor filters and phase symmetry, and then to extract the region with similar direction information by entropy.

For fat layer detection, we propose an automatic thresholding approach in collaboration with topological relation information.

Once the fat and muscle layers are determined, the hypoechoic regions in-between these two layers are more likely to be a breast lesion. The second step is to use the in-between regions to detect lesions.

The basic idea of this article is different from other publications (we will mention in Chapter 2) that detect lesions on whole ultrasound images; it detects lesions in the region with a high probability that lesions exist. It can increase the accuracy rate of lesion detection and apply to cysts, benign and malignant lesions. This proposed algorithm can also be combined with other lesion detection algorithms to decrease the false positive rate and improved to provide more important information to clinical applications.

1.5 Data source

The 2-D breast ultrasound images we use to implement this algorithm in this thesis are from Doctor Wen-Hong Guo in the department of surgery at National Taiwan University Hospital (NTUH) and Doctor Yi-Hong Chou in the department of radiology at Taipei Veterans General Hospital (TGHV).

We are deeply appreciative of their help in surveying the accuracy of our algorithm.



Chapter 2

Reference literature

Recently, there are several studies about computer-aided detection (CAD) system for lesion detection on ultrasound images. This chapter illustrates several important approaches of this topic, such as the radial gradient index, skewness, the Canny edge detector, and so on.



Computer-aided detection (CAD) methods have been explored by various researchers in single breast ultrasound images [11] - [15]. Several related literatures are mentioned here.

Drukker, et al. proposed two methods. In 2002, Drukker, et al. proposed a method to use the radial gradient index (RGI), which estimates shape and gray level information of lesions to identify the benign breast lesion [12].

The definition of RGI is

$$RGI_i(x, y) = \frac{1}{\sum_{(x', y') \in C_i} |\vec{g}(x', y')|} \sum_{(x', y') \in C_i} \vec{g}(x', y') \cdot \hat{r}(x', y') \quad (2.1)$$

where

$\vec{g}(x', y')$: the (maximum) gradient vector of gray level value.

$|\vec{g}(x', y')|$: the length of $\vec{g}(x', y')$.

$\hat{r}(x', y')$: the unit radial vector which points from center (x, y) to the boundary point (x', y') of the contour C_i .

In 2003, Drukker, et al. proposed a method to detect posterior acoustic shadowing effect based on skewness, in this method which the posterior acoustic shadowing effect is an indicator for the malignant breast lesion [13].

Skewness can be estimated by the third central moment, and the definition of the skewness is

$$S(x, y) = \frac{1}{N} \sum_{(x', y') \in A} \frac{(h(x', y') - \langle h(x', y') \rangle)^3}{\sigma_A^3} \quad (2.2)$$

where

A : a rectangular ROI with center (x, y) .

σ_A : the standard deviation of the gray level value distribution in A .

N : the number of the total points in A .

$h(x', y')$: the gray level of position (x', y') in the image.

$\langle h(x', y') \rangle$: the mean gray level of the total points in A .

The relation between an original image, a center (x, y) of A , and A is shown in Fig 2.1.

2.1.

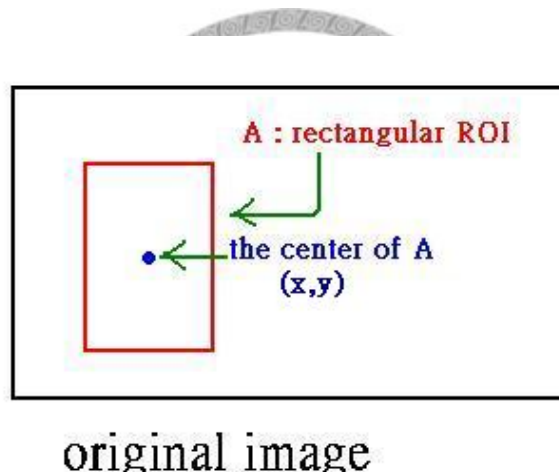


Fig 2.1 This figure shows the relation of the variables original image, the center (x, y) of A , and the rectangular ROI A of skewness.

Ikedo, et al. proposed to use a Canny edge detector to estimate the vertical edges in ultrasound image [14]. The Canny edge detection is defined as :

$$\theta(x, y) = \arctan \frac{f_y(x, y)}{f_x(x, y)} \quad (2.3)$$

where

$\theta(x, y)$: the direction of the gray level gradient at (x, y) .

$f_x(x, y)$: x -direction differential value.

$f_y(x, y)$: y -direction differential value.

and the edge direction at (x, y) is

$$d(x, y) = \theta(x, y) + \frac{\pi}{2} \quad (2.4)$$

They suggested that a region with more vertical edges is more likely to be a lesion.

An example is shown in Fig 2.2.

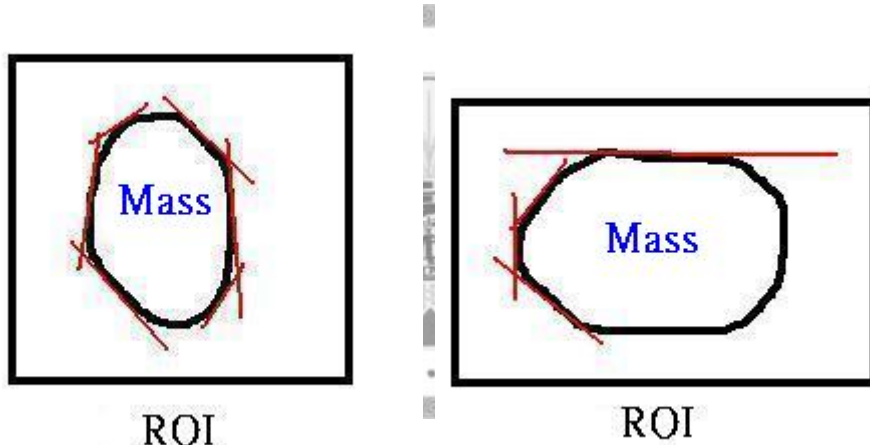


Fig 2.2 Concept of a Canny edge detector. A mass is identified by two vertical edges (as the left figure shows) or a vertical edge and a horizontal edge (as the right figure shows).

RF Chang, et al. proposed the article, "Whole breast computer-aided screening using free-hand ultrasound [15]." This article mentions four features to identify a breast lesion in a single breast ultrasound image. These four features are darkness, uniformity, width-height ratios, and region area size.

A region R is considered as suspicious tissue because it can satisfy these four criteria described in the following.

- Darkness :

$$Avg_R = \frac{\sum_{(x,y) \in R} G_R(x, y)}{M} \quad (2.5)$$

$G_R(x, y)$: the gray level of point (x, y) in R .

M : the number of the total points in R .

Avg_R : the mean gray level of the total points in R .

- Uniformity :

$$Var_R = \frac{\sum_{(x,y) \in R} (G_R(x, y) - Avg_R)^2}{M} \quad (2.6)$$

Var_R : the difference of the magnitude of Avg_R and the gray level value of each point of R .

- Width-height ratio :

As $H_R > W_R$,

$$R_{WH} = \frac{W_R}{H_R} \quad (2.7)$$

H_R : height of R , that is y -direction difference of R .

W_R : width of R , that is x -direction difference of R .

- Region area size : $Area_R$ is the number of the total points in R .

There are four thresholds for these four features, respectively. Because the region R that can satisfy these four criteria is considered as suspicious tissue, it is highly probable to think R to be a lesion or cyst.

Madabhushi, et al. proposed a method to use a probability model to estimate the position of lesions; it means that use features of lesions to train a probability model [11]. The feature information includes a gray level value, texture and position of lesions. The definition of probability model is

$$\tau_{C_{x,y}} = \frac{\Gamma_{C_{x,y}}(i,t) J_{C_{x,y}} Y_{C_{x,y}}}{d_{C_{x,y}}} \quad (2.8)$$

$$\Gamma(i,t) = \Gamma(i)\Gamma(t) \quad (2.9)$$

where

$C_{x,y}$: a point of the image.

$\Gamma(i,t) = \Gamma(i)\Gamma(t)$, $\Gamma(i)$ and $\Gamma(t)$ are independent.

$\Gamma(i)$: the probability distribution of a gray level of inside lesions.

$\Gamma(t)$: the probability distribution of a texture, which is the gray level difference between one point and the mean gray level of its neighborhood.

$J_{C_{x,y}}$: the mean $\Gamma_{C_{x,y}}(i,t)$ of the neighborhood of $C_{x,y}$

$Y_{C_{x,y}}$: the distance between $C_{x,y}$ and the bottom of the image.

$d_{C_{x,y}}$: the distance between $C_{x,y}$ and the center of the image.

If $\tau_{C_{x,y}}$ value is larger, there is a higher probability that $C_{x,y}$ is one part of a tumor.

Compared with the methods mentioned above, a method combining more information about breast anatomic information and features of lesions would provide higher accuracy of lesion detection.

Chapter 3

Method and Material

This chapter proposes anatomic information to process original ultrasound images. This algorithm includes three parts: muscle layer detection, fat layer detection, and lesion detection. We fulfill these three steps by using the Gabor filters, phase symmetry, the entropy concept, and automatic threshold selection. This chapter will illustrate them individually to show the derivation of the algorithm.



The basic idea of this article is to separate the fat layer, the breast tissue and the muscle layer in a single breast ultrasound image based on the texture of each part, respectively.

Texture of the muscle layer, rich in horizontal strips, is even symmetric characteristic for the human visual effect. Identifying the region with a specific direction is one topic of image phase information, which will be discussed later. In this thesis, we use the Gabor filters to define a phase symmetry (PS) indicator; it means that we use the Gabor filters to a model response field of simple cells in a V1 area and then phase symmetry (PS) as an indicator to quantify the phase symmetry property in the vicinity of each pixel. After using the Gabor filters and phase symmetry, the result we obtain is called PS map. One can create normalized weighting angle distribution according to information of a PS map, and then compute entropy of normalized weighting angle distribution of each region in the PS map to identify a muscle layer area.

Texture of the fat layer is dark and connected regions in upper part of an ultrasound image, thus we can use a thresholding-based approach and utilize topological relation information to identify the fat layer region.

Finally we detect lesions only in the breast tissue region with a high probability of occurrence of lesions, and identify lesions based on the gray level, region size, position, and other information.

Image phase information is a clue component to provide more information about the visual appearance than does image magnitude information in the interpretation of a scene [16]. A seminal paper proposed to use a local energy model to detect phase-based features, and in the signal the features are perceived at points where those phase components of Fourier are maximal, which is equivalent to where phase congruency (PC) are maximal

[17]. It is why image phase information has been researched broadly as a foundation indicator for feature detection in several image data [18] - [22]. In this article, we propose to use local phase information to accurately and robustly detect the muscle layer of breast structures in ultrasound images.



3.1 Gabor Filter-Extract local phase information based on image feature

Vision is a very complex procedure in human brain. Although extensive studies have been carried out in an attempt to achieve better understanding of the visual process for decades, the outcomes are still entirely limited. Recent researches on psychophysiology, psychophysics, and neurology have proposed that simple cells are the fundamental processing components of visual information. The receptive field profile of a simple cell in the V1 area would be modeled as an even or an odd Gabor filter, and each simple cell is tuned to a specific narrow frequency and orientation band to capture particular local signal properties [23]. The inputs of a simple cell are nearly added up and weighted by the response of the corresponding Gabor filter coefficients. The output of a simple cell is half-way rectified.

The receptive field profile of the primary visual cortex may also be produced by other models such as DOG (i.e., difference of Gaussians) model non-oriented cells [24], and DOOG (i.e., the difference of offset Gaussians) [25]. The DOOG function is a linear combination of three offset identical Gaussian functions. The zero-mean Gaussian function in the spatial domain is defined as :

$$G(x_0, y_0, \sigma_x, \sigma_y) = \frac{1}{2} \pi \sigma_x \sigma_y \times \exp\left\{-\frac{(x - x_0)^2}{\sigma_x^2} + \frac{(y - y_0)^2}{\sigma_y^2}\right\} \quad (3.1.1)$$

where

σ_x : the standard deviations in the x direction

σ_y : the standard deviations in the y direction

(x_0, y_0) : the center of the Gaussian function

As an example, the DOOG function used in this paper [25] is :

$$DOOG = a \cdot G(0, y_a, \sigma_x, \sigma_y) + b \cdot G(0, y_b, \sigma_x, \sigma_y) + c \cdot G(0, y_c, \sigma_x, \sigma_y) \quad (3.1.2)$$

where

$$y_a = -y_c = \sigma_y$$

$$y_b = 0$$

For an ultrasound image, because the textures of the muscle layer are not only complex but also irregular, the significant frequency components of the whole image do not necessarily correlate with the principal spatial frequency components of the textures. Therefore, in an ultrasound image a reasonable choice would be to use a predefined set of receptive field profiles with a reasonably specific frequency and orientation in the frequency domain. Therefore, we can use specific frequency and orientation Gabor filters to model visual information.

The general form of a 2D Gabor filter may be expressed by :

$$g(x, y) = \exp\{-(x - x_0)^2/a^2 + (y - y_0)^2/b^2]\pi\} \times \exp\{-2\pi i[u_0(x - x_0) + v_0(y - y_0)]\} \quad (3.1.3)$$

where

a : the standard deviations in the x direction

b : the standard deviations in the y direction

The Fourier transform is defined as :

$$G(u, v) = \exp\left\{-\frac{1}{\pi}\left[\frac{(u - u_0)^2}{\sigma_u^2} + \frac{(v - v_0)^2}{\sigma_v^2}\right]\right\} \times \exp\{-2\pi i[x_0(u - u_0) + y_0(v - v_0)]\} \quad (3.1.4)$$

where

σ_u : the standard deviations in the u direction

σ_v : the standard deviations in the v direction

The Gabor filter has a good property to achieve the lower bounds of the two uncertainty inequalities $\Delta x \bullet \Delta u \geq \pi/4$ and $\Delta y \bullet \Delta v \geq \pi/4$ simultaneously. That is to say, it may achieve very narrow frequency and orientation responses while spatial localization is maintained.

One can estimate localization of spatial and frequency signal information simultaneously by constructing a set of quadrature filters, called filter bank including different frequency or orientation of the used Gabor filters. The filter bank is constructed at different frequencies which are multiples of a minimum user-defined wavelength λ_{\min} ; $\Delta\theta$ is the angular separation between neighboring orientations and defined as $\Delta\theta = 180^\circ/N_\theta$, where N_θ is the total number of orientations set we used to define specific frequencies.

A general Gabor filter combines an even Gabor filter and an odd Gabor filter. The even Gabor filter is a Gaussian filter convolves a cosine function in the spatial domain and in the frequency domain, and it is a pair of symmetric Gaussian filters. The odd Gabor filter is a Gaussian filter convolves a sine function in the spatial domain and in the frequency domain, and it is a pair of anti-symmetric Gaussian filters.

There is an example about two Gabor filters of the same frequency but different orientations, as shown in Fig 3.1.1.

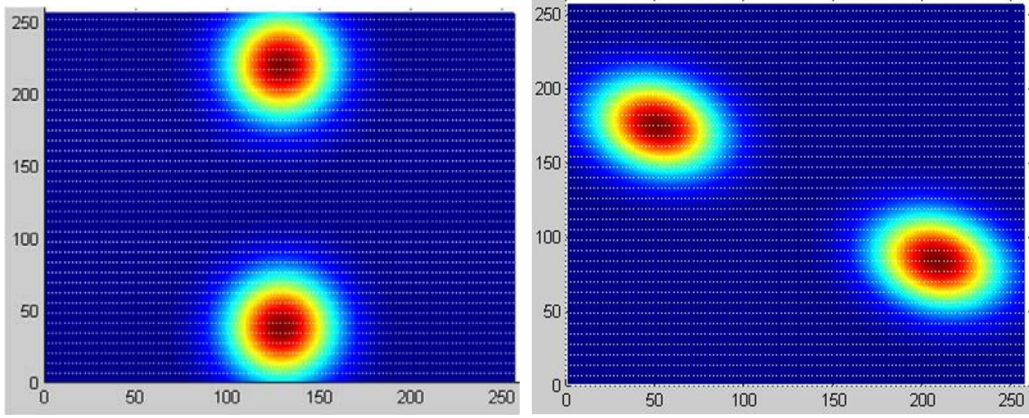


Fig 3.1.1 An example of two different orientation even Gabor filters. The left figure shows the responses of an even filter in the frequency domain, the center frequency is $64\sqrt{2}$ and the orientation is 0^0 . The right figure also shows the responses of an even filter in the frequency domain, the center frequency is the same as the left figure, but the orientation is different, and it is 30^0 .

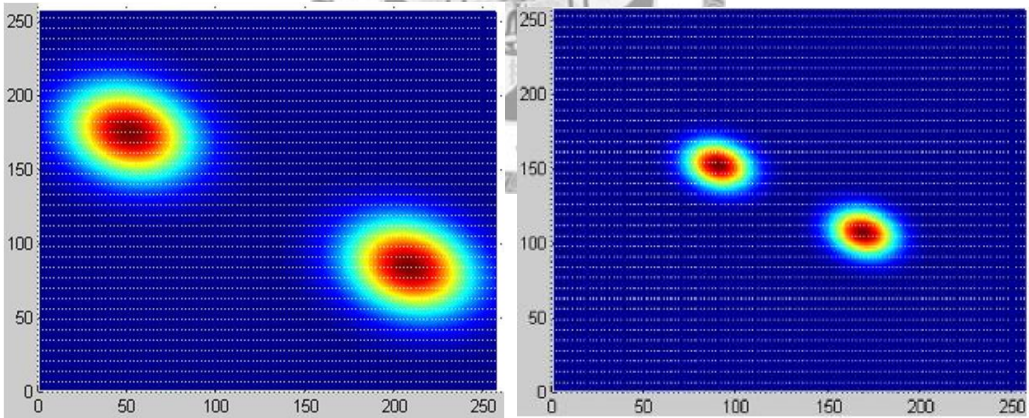
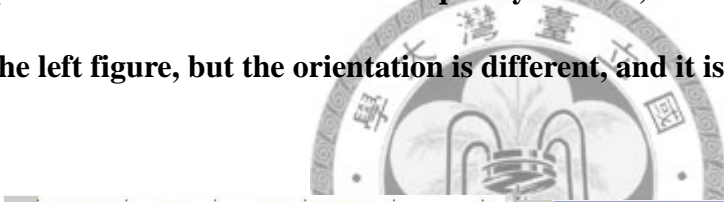


Fig 3.1.2 An example of two different frequency even Gabor filters. The left figure shows the responses of an even filter in the frequency domain, the center frequency is $64\sqrt{2}$ and the orientation is 30^0 . This figure is the same as the right figure in Fig.3.1.1. The right figure also shows the responses of an even filter in the frequency

domain, the center orientation is the same as the left picture, but the frequency is different, and it's $32\sqrt{2}$.

Another example about two Gabor filters with the same orientation but different frequencies is given, as shown in Fig 3.1.2.

Another example about the set of Gabor filters in the frequency domain, which is called a rosette map employed in this study [26], is shown in Fig 3.1.3. In Fig 3.1.3, each ellipse is a Gaussian filter in the frequency domain, and each pair of ellipses symmetrical with respect to the origin (the center) represents an even Gabor filter; it means an even Gabor filter is a pair of symmetric Gaussian filters.

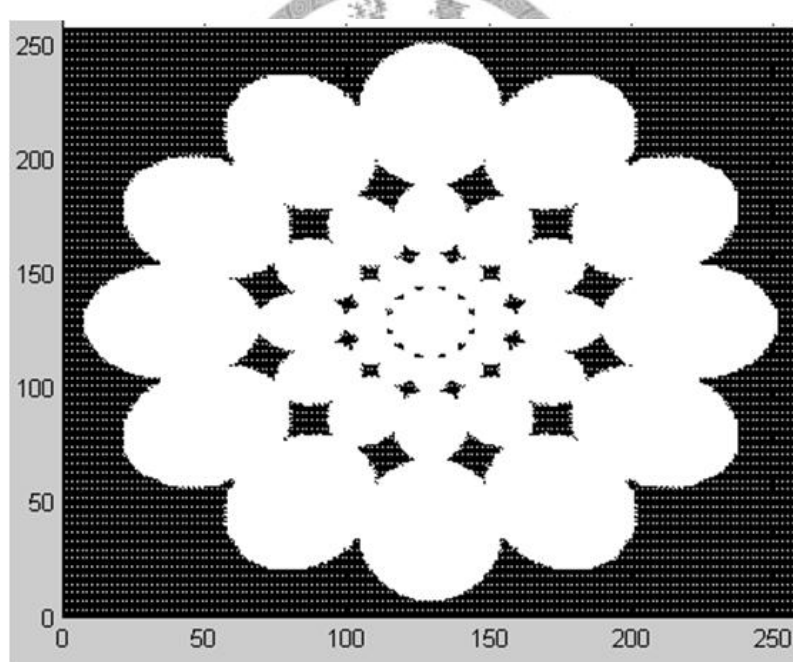


Fig 3.1.3 This figure presents a Rosette map which are sets of Gabor filters of a specific frequency and orientation in the frequency domain. Each Gabor filter consists of two Gaussian filters (a pair of ellipses in this figure) symmetrical with respect to the origin (DC component, i.e., the center) represents an even Gabor filter.

The figure only shows the portion larger than the half-peak magnitude of each Gaussian filter.

For the horizontal pairs of Gaussian filters, the frequency bandwidth B_f (the bandwidth in the horizontal (radial) direction), and the orientation bandwidth B_θ (the bandwidth in the azimuthal direction) are defined as [26]

$$B_f = \log_2 \left(\frac{u_0 + (2 \ln 2)^{1/2} \sigma_u}{u_0 - (2 \ln 2)^{1/2} \sigma_u} \right) \quad (3.1.5)$$

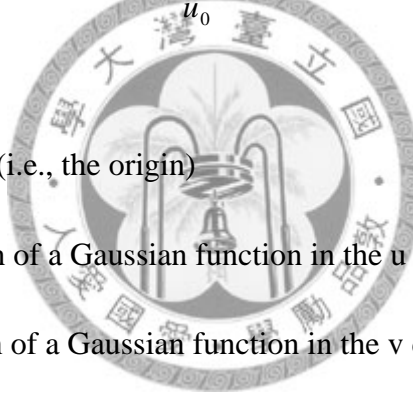
$$B_\theta = 2 \tan^{-1} \left(\frac{(2 \ln 2)^{1/2} \sigma_v}{u_0} \right) \quad (3.1.6)$$

where

u_0 : the central frequency (i.e., the origin)

σ_u : the standard deviation of a Gaussian function in the u dimension

σ_v : the standard deviation of a Gaussian function in the v dimension



The bandwidth is estimated to be associated with the half-peak magnitude for each Gabor filter.

In this article, we both use the even and odd Gabor filters, which are quadrature filters for each other. A quadrature filter can be used to identify local phase information through estimation of the amplitude and phase of the specific frequency and orientation signal at a given spatial location.

The odd Gabor filter is similar to the even Gabor filter, but it is a pair of anti-symmetric Gaussian filters, as an example shown in Fig 3.1.4.

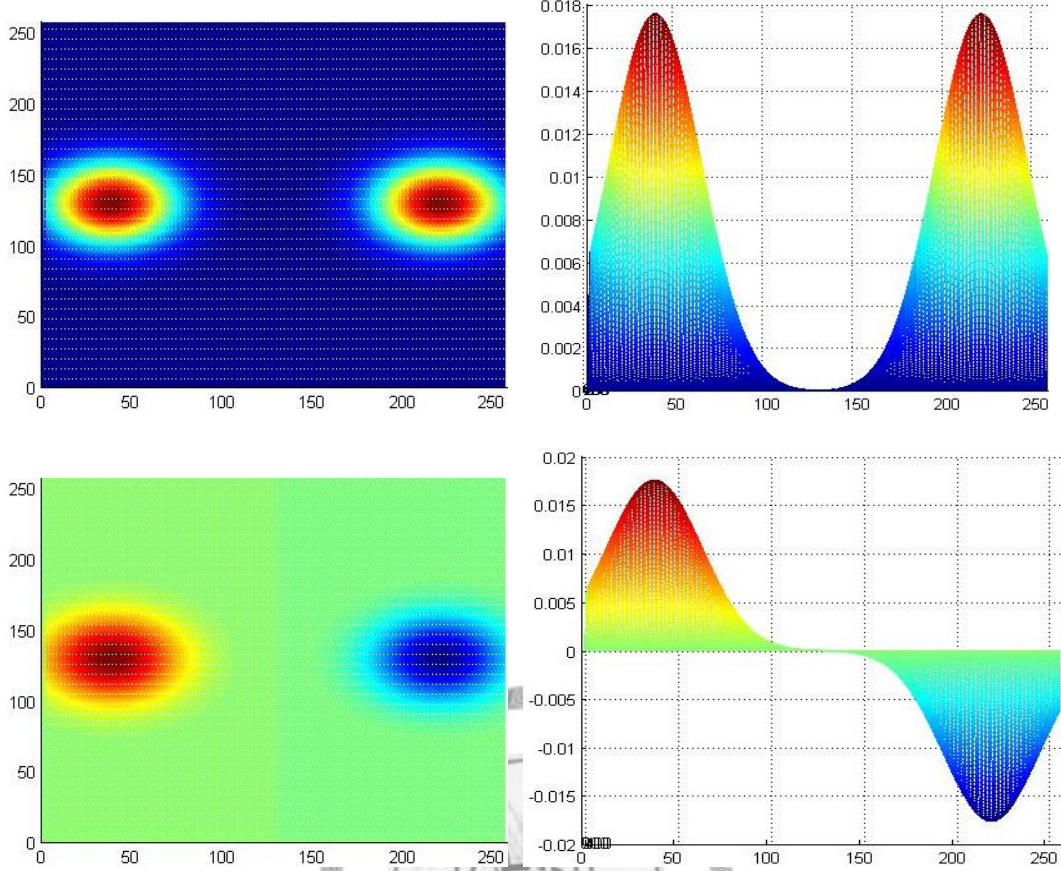


Fig 3.1.4 Comparison between the even and odd Gabor filters. The left upper figure is an even filter in the frequency domain, and the right upper figure is the magnitude of the even filter. The left lower figure is an odd filter in the frequency domain, and the right lower figure is the magnitude of the odd filter. This example shows the difference between the even and odd Gabor filters. The even Gabor filter is symmetric, and the odd Gabor filter is anti-symmetric.

For a specific frequency f and orientation θ , a Gabor filter can be represented as

$$M_{f,\theta}^e(x, y) = \text{real}(F^{-1}(G_{f,\theta})) \quad (3.1.7)$$

$$M_{f,\theta}^o(x, y) = \text{imag}(F^{-1}(G_{f,\theta})) \quad (3.1.8)$$

where

$M_{f,\theta}^e(x, y)$: the spatial even-symmetric (i.e., cosine) Gabor filter

$M_{f,\theta}^o(x, y)$: the spatial odd-symmetric (i.e., sine) Gabor filter

$I(x, y)$: the spatial image

F^{-1} : the inverse Fourier transform

Consider the responses of each set of quadrature filters as a vector :

$$[e_{f,\theta}(x, y), o_{f,\theta}(x, y)] = [I(x, y) * M_{f,\theta}^e(x, y), I(x, y) * M_{f,\theta}^o(x, y)] \quad (3.1.9)$$

where

$e_{f,\theta}$: imagined as real part of a complex valued spatial component

$o_{f,\theta}$: imagined as imaginary part of a complex valued spatial component.



For a specific frequency f and orientation θ Gabor filter also be described as

$$A_{f,\theta}(x, y) = \sqrt{e_{f,\theta}(x, y)^2 + o_{f,\theta}(x, y)^2} \quad (3.1.10)$$

$$\phi_{f,\theta}(x, y) = \tan^{-1}(o_{f,\theta}(x, y), e_{f,\theta}(x, y)) \quad (3.1.11)$$

$$E(x, y) = \sqrt{\left(\sum_f \sum_\theta e_{f,\theta}(x, y)\right)^2 + \left(\sum_f \sum_\theta o_{f,\theta}(x, y)\right)^2} \quad (3.1.12)$$

where

$A_{f,\theta}(x, y)$: the amplitude

$\phi_{f,\theta}(x, y)$: the local phase

$E(x, y)$: the local energy function

The different responses exist due to a set of frequency and orientation Gabor filters for each point (x, y) in an image $I(x, y)$. We will describe the visual effect representation of the responses of the even and odd Gabor filter in the next section.



3.2 Phase Symmetry-Quantify the symmetry property of a point

As we mentioned above, in a breast ultrasound image, a muscle layer seems blurred and irregular because of speckle noise, artificial effect, and posterior acoustic shadowing. The texture of the muscle layer is rich in horizontal strips; for human visual effect is even symmetric property. It is much better to use a ridge-like technique to depict strips in ultrasound responses than using other techniques, like using line-profiled technique to model a muscle layer. This article proposes a ridge detector as a receptive feature for detection of muscle layer localization in a breast ultrasound image, and the purpose of the ridge detection is to capture the principal axis of the strip symmetry of a muscle layer.

The patterns are even symmetric to the center, and their Fourier transforms are real (and even); the patterns are odd symmetric to the center, and their Fourier transforms are imaginary (and odd). If the patterns are neither perfectly odd symmetric nor perfectly even symmetric, their Fourier transforms are complex value, of which the magnitude combines real and imaginary value, and the phase values reflect the degree of symmetry. Local phase information is evaluated by (3.1.8), (3.1.9), and (3.1.10).

While a point whose vicinity has symmetric texture pattern characteristic in images, the absolute value of the even-symmetric filter outputs (e.g., even Gabor filter $e_{f,\theta}(x, y)$) will be large, while the absolute value of the odd-symmetric filter outputs (e.g., odd Gabor filter $o_{f,\theta}(x, y)$) will be small [20], and the even Gabor filter dominates the odd Gabor filter. An example is provided to explain the estimation of an image with the even and odd Gabor filters in Fig 3.2.1 to Fig 3.2.3.

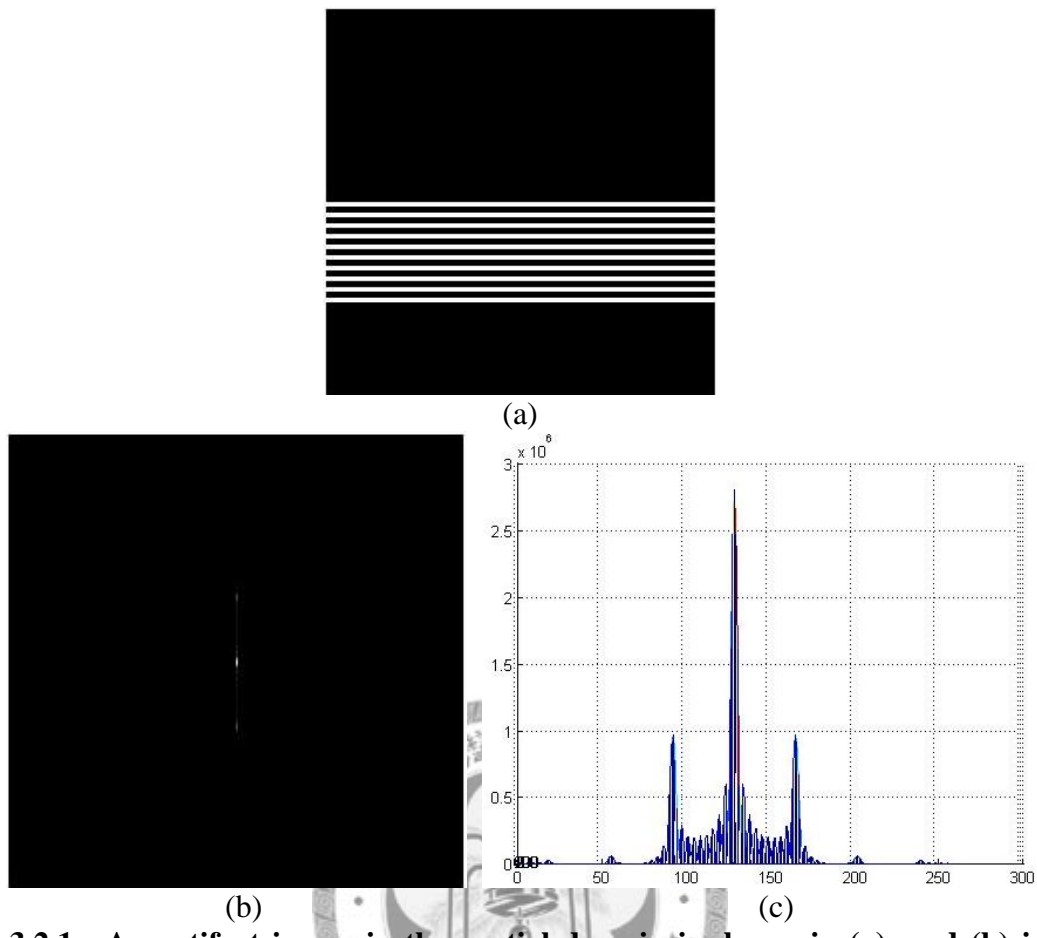


Fig 3.2.1 An artifact image in the spatial domain is shown in (a), and (b) is its Fourier transform form in frequency domain. (c) shows the absolute magnitude of (b).



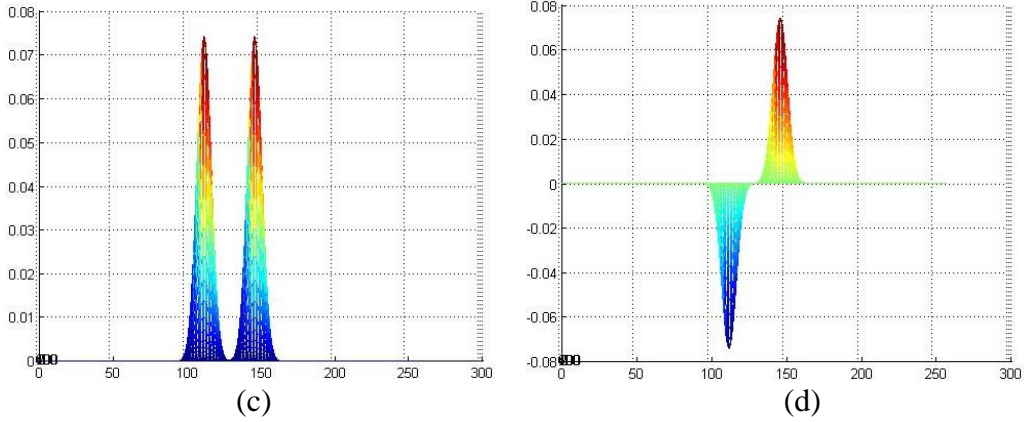
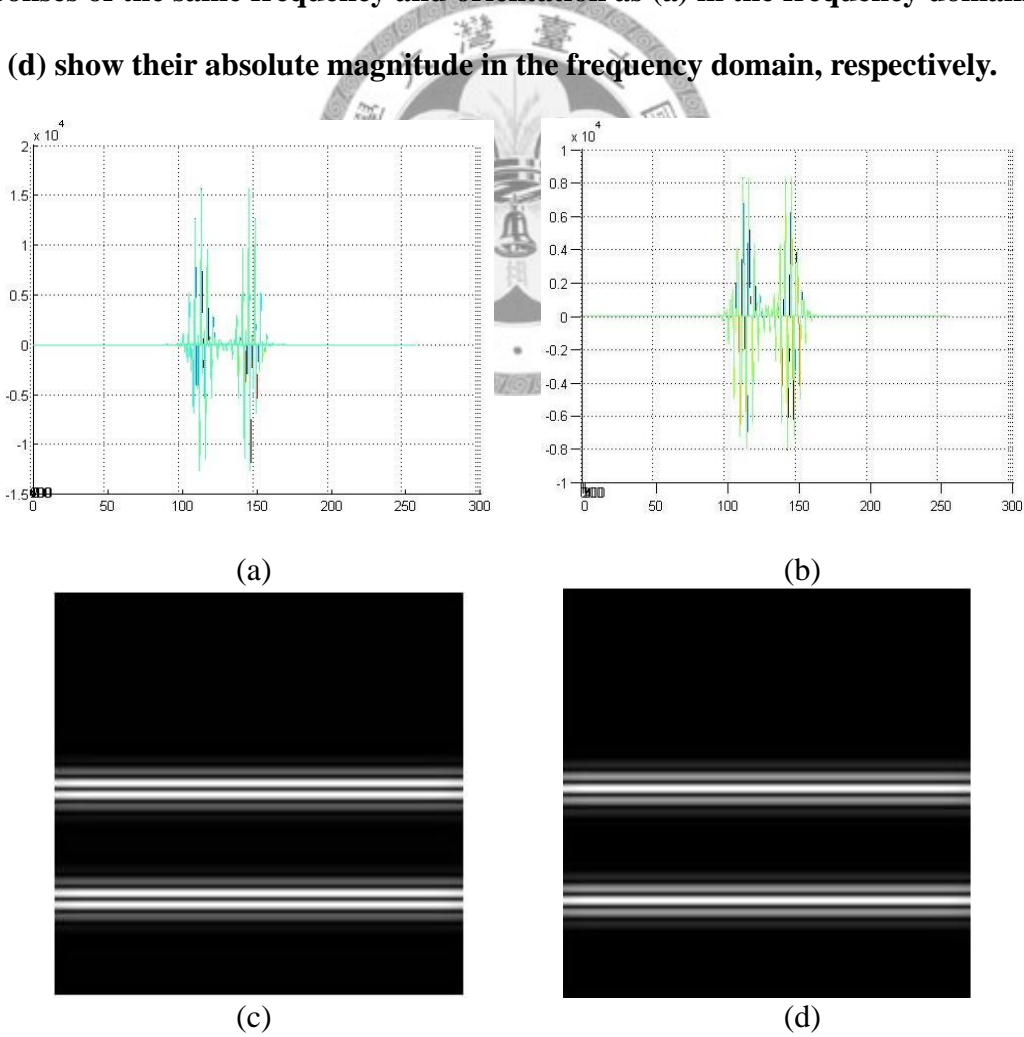


Fig 3.2.2 (a) and (c) represent even Gabor filter responses, and (b) and (d) odd Gabor filter responses. (a) shows even Gabor filter responses of the specific frequency and orientation in the frequency domain. (b) shows the odd Gabor filter responses of the same frequency and orientation as (a) in the frequency domain. (c) and (d) show their absolute magnitude in the frequency domain, respectively.



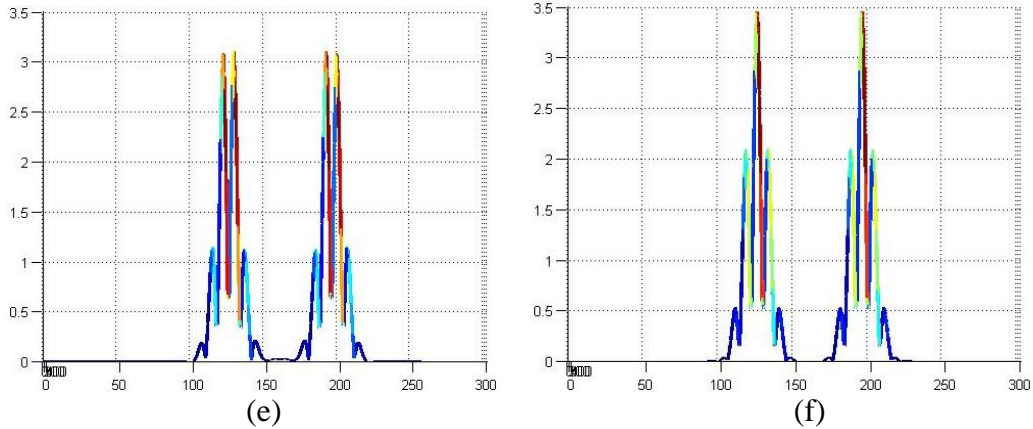
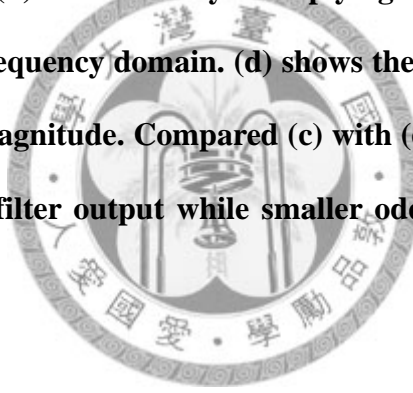


Fig 3.2.3 The processed images obtained by using the preceding even and odd Gabor filters: (a) is derived by multiplying the original image with the even Gabor filter in the frequency domain. (c) shows the inverse Fourier transform of (a), and (e) shows its magnitude. (b) is derived by multiplying the original image with the odd Gabor filter in the frequency domain. (d) shows the inverse Fourier transform of (b), and (f) shows its magnitude. Compared (c) with (d), it is clear that one point have larger even Gabor filter output while smaller odd Gabor filter output, vice versa.



There is a method to quantify symmetry by taking the difference between absolute value of the even-symmetric filter (even Gabor filter) output and the absolute value of the odd-symmetric filter (odd Gabor filter) output. It is equivalent to take the difference of the absolute value of phase angle cosine value and sine value; the difference varies phase deviation nearly linear and between ± 1 .

The difference can be basically normalized by the sum of magnitude differences between even Gabor filter output and odd Gabor filter output over multiple frequencies and orientations. Herein, the magnitude differences are normalized by the magnitude of the response vector of the even Gabor filter and odd Gabor filter at each frequency and

orientation. A measure of phase symmetry (PS) is :

$$PS(x, y) = \frac{\sum_f \sum_{\theta} \left| |e_{f,\theta}(x, y)| - |o_{f,\theta}(x, y)| \right| - T_r}{\sum_f \sum_{\theta} \sqrt{|e_{f,\theta}|^2(x, y) + |o_{f,\theta}|^2(x, y)} + \varepsilon} \quad (3.2.1)$$

where

$$\lfloor A \rfloor = \max(A, 0).$$

ε : a small constant included to avoid division by zero while the signal is uniform and

derives no filter response.

T_r : an orientation-dependent noise threshold term. It describes the strongest noise

response, which could be generated from the signal. T_r is defined as $T_r = \mu + k\sigma$,

and for ultrasound data, the distribution is expected to be Rayleigh distribution [27].

T_r is derived by combining noise influences on each filter, estimations which are calculated by the mean (μ) of the local energy distribution, due to noise, plus a specific constant (k) multiplied by standard deviations (σ) [28]; μ and σ are evaluated by the response of the smallest frequency filter.

For a specific orientation, the response of the smallest frequency filter is used to estimate an independent noise compensation term of each orientation. k would be tuned to balance the relation between the detected muscle layer texture and the speckle noise for different ultrasound machine settings. More details about the phase symmetry technique are mentioned in those papers [17][19][28][29].

After using the even and odd Gabor filters and phase symmetry, one can obtain local phase information of an image, which is so clear to assist to detect the region

robustly. In this article, the result we get called a PS map was shown in Fig 3.2.2. The direction information is enhanced in a PS map, which is clearer than the original image. The difference between the muscle layer location and the other tissue of the breast location in a PS map is clear, the muscle layer location possesses more similar direction information and other tissue possesses various direction (i.e., dissimilar direction) information.

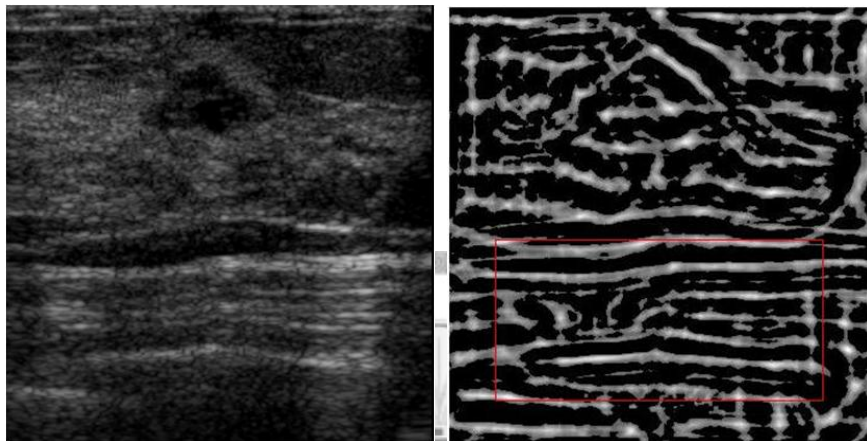


Fig 3.2.4 Here presents an example about a PS map. The left figure is original image. After using the Gabor filters and phase symmetry, we derive the result which called a PS map, shown the right figure. The region with red edge is the location of muscle layer where are with more and clearer horizontal direction information than the original image. In right figure, the difference between muscle layer and other tissue is clear.

3.3 Entropy-Identify perplexity of direction information in a region

The information theory is an essential tool to deal with information representation and manipulation quantitatively and directly. In this article, we examine the application of this tool of specific problems of image processing about detection information of a muscle layer in ultrasound images.

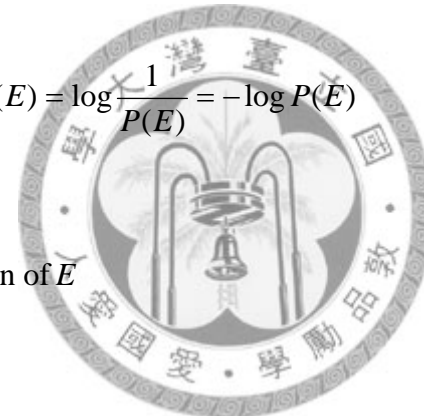
The basic hypothesis of the information theory is that the generation of information is modeled as a probabilistic procedure, which could be estimated in an intuitive way.

A random event E would occur with probability $P(E)$, and the information of E is

$$I(E) = \log \frac{1}{P(E)} = -\log P(E) \quad (3.3.1)$$

where

$I(E)$: the self-information of E



That means a random event E with an occurred probability $P(E)$ contains $I(E)$ units of information.

In the case that the event E always occurs; it means $P(E)=1$, and the $I(E)=0$, that is no information attributed from E owing to no uncertainty associated with the event E . In this situation no information would be delivered while the event E has occurred. In other case that the event E does not frequently occur as above, likely implying $P(E)=0.9$; some small amount of information would be delivered while the event E has occurred. It provides more information when the communicating event E has not occurred, because the outcome is not apt to predict. The relation between $I(E)$

and $P(E)$ is inverse proportion.

The average information per source output, denoted $E\{I(x)\}$, which is

$$\text{Entropy} = E\{I(x)\} = -\sum_i p(x_i) \ln p(x_i) \quad (3.3.2)$$

where

$I(x)$: information of x

$p(x)$: probability of occurrence of x

$E\{I(x)\}$ is frequently called the uncertainty or entropy of the source, which describes a state of the required average amount of information to observe a single source output. Entropy is a measure of the uniformity of the distribution of energy. The source events are uniform distribution; it means they have an equal probability and the uncertainty or entropy is maximized for this case. Each source event conveys the splendid possible average information. If the magnitude of entropy increases, the source conveys the more information.

The texture of the muscle layer in an ultrasound image is rich in horizontal strips, which means more points in the muscle layer region have similar direction information.

In this article, we use entropy to estimate the weighting angle distribution of the PS map, which is derived from computing the Gabor filters and phase symmetry in a breast ultrasound image. The weighting angle distribution is obtained from computing the direction and magnitude of each pixel of the region whose size is defined by a user, e.g. 32×32. For each pixel of a pattern in the PS map, adding the magnitude value of all pixels in accordance with its orientation products a weighting angle distribution.

We suppose that the magnitude value stands for the dependence of the direction in

PS map. The magnitude value is larger, it can be convinced more; the magnitude value is smaller or not easy to perceive, it can not be convinced less or not providing information.

Normalizing the weighting angle distribution by the sum of all magnitude of each pattern, we can obtain a normalized weighting angle distribution to estimate the entropy. Entropy of the weighting angle distribution is larger if more points in the given region have dissimilar direction information, as shown in the first example; on the contrary, entropy of weighting angle distribution is smaller if more points in the given region have similar direction information, as shown in the second example. The example about weighting angle distribution is shown in Fig 3.3.1.



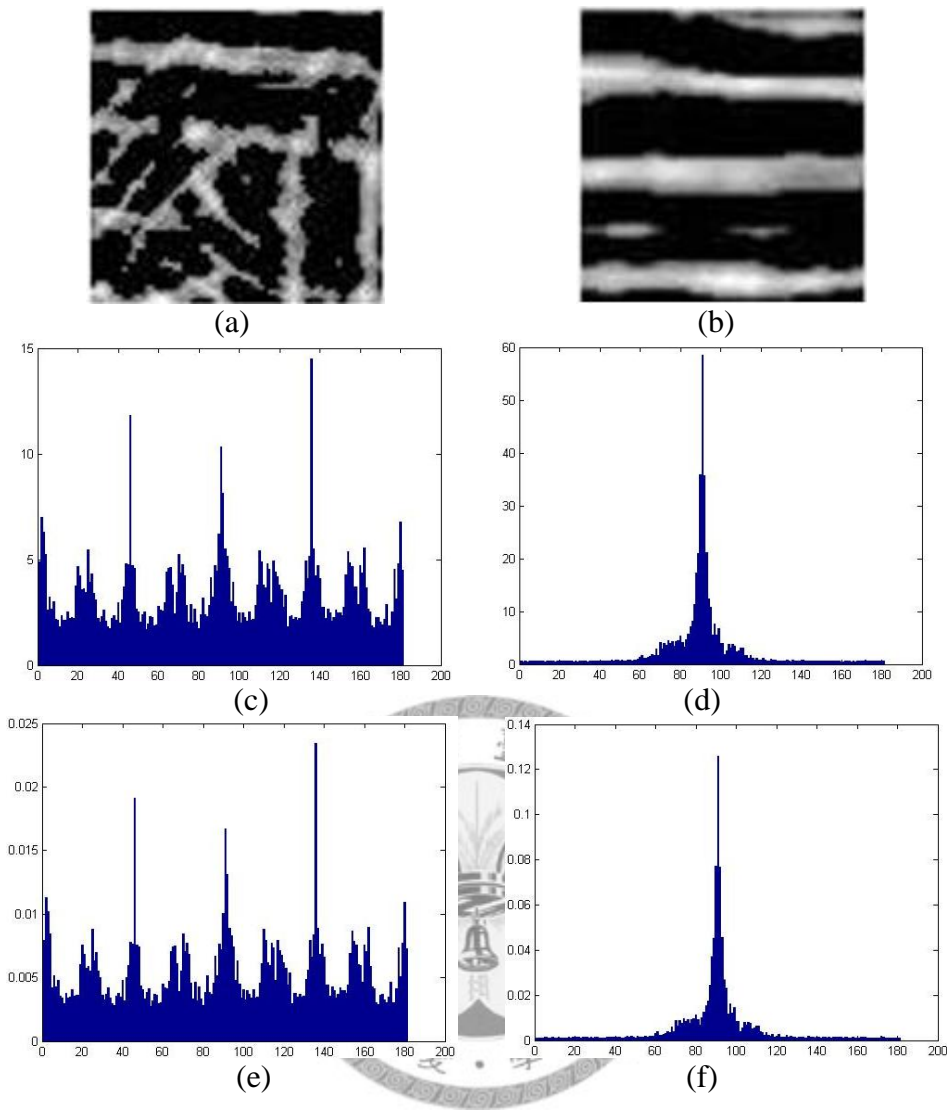


Fig 3.3.1 There are two examples to interpret weighting angle distribution of patterns. (a), (c), and (e) show the first example, and (b), (d), and (f) show the second example. (a) and (b) show original patterns; (c) and (d) show the diagram of weighting angle distribution of the original patterns; (e) and (f) are the normalized weighting angle distribution of (c) and (d), respectively. For the weighting angle distribution, the horizontal axis and the vertical axis mean the degree and magnitude of each pixel, respectively. Note that the vertical axis shows the summed magnitude value of the all pixels in accordance with the degree bin of each pixel, and the weighting angle distribution of each pattern is normalized by the sum of

all magnitude of the corresponding pattern to compute the entropy. Entropy of the weighting angle distribution is larger if more points in the given region have dissimilar direction information, as shown in the first example; on the contrary, entropy of weighting angle distribution is smaller if more points in the given region have similar direction information, as shown in the second example.

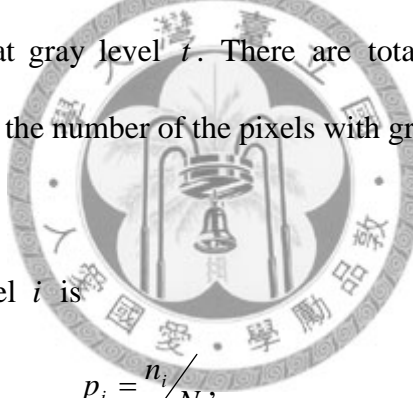


3.4 Thresholding- automatic multi-level classification

Image thresholding plays an important role in applications of image processing because of its simple implementation. Using thresholding technique to identify and derive an object from the distribution of gray levels or texture in an image is practical and common. In this article, we implement automatic thresholding selection in many situations to classify each distribution.

The study proposed a nonparametric and unsupervised method of automatic threshold selection for image processing [30]. For example, one can divide all the pixels in an image, which is a 2-D gray level intensity function, into two classes C_1 and C_2 , according to a threshold at gray level t . There are total N pixels with gray levels $[1,2,\dots,L]$ in the 2-D image, the number of the pixels with gray level i is denoted n_i , so

$$N = n_1 + n_2 + \dots + n_L.$$



The probability of gray level i is

$$p_i = \frac{n_i}{N}, \quad (3.4.1)$$

$$p_i \geq 0 \quad \text{and} \quad \sum_{i=1}^L p_i = 1$$

For the first class C_1 with gray levels $[1,\dots,t]$:

$$\omega_1(t) = p_r(C_1) = \sum_{i=1}^t p_i \quad (3.4.2)$$

The gray level probability distribution for this class is the sum of $\frac{p_1}{\omega_1(t)}, \dots, \frac{p_t}{\omega_1(t)}$:

$$\mu_1 = \sum_{i=1}^t i P_r(i|C_1) = \sum_{i=1}^t i p_i / \omega_1(t) \quad (3.4.3)$$

$$\sigma_1^2 = \sum_{i=1}^t (i - \mu_1)^2 P_r(i|C_1) = \sum_{i=1}^t (i - \mu_1)^2 p_i / \omega_1 \quad (3.4.4)$$

For the second class C_2 with gray levels $[t+1, \dots, L]$:

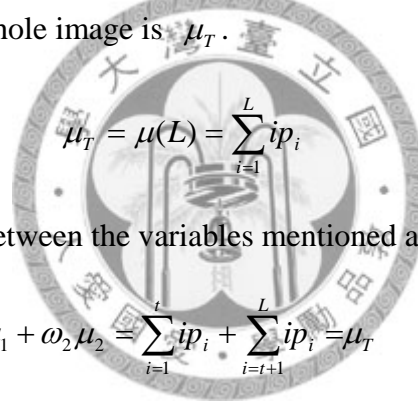
$$\omega_2(t) = P_r(C_2) = \sum_{i=t+1}^L p_i \quad (3.4.5)$$

The gray level probability distribution for this class is the sum of $p_{t+1} / \omega_2(t), \dots, p_L / \omega_2(t)$:

$$\mu_2 = \sum_{i=t+1}^L i P_r(i|C_2) = \sum_{i=t+1}^L i p_i / \omega_2(t) \quad (3.4.6)$$

$$\sigma_2^2 = \sum_{i=t+1}^L (i - \mu_2)^2 P_r(i|C_2) = \sum_{i=t+1}^L (i - \mu_2)^2 p_i / \omega_2 \quad (3.4.7)$$

The mean gray level for whole image is μ_T .



$$\mu_T = \mu(L) = \sum_{i=1}^L i p_i \quad (3.4.8)$$

There are some relations between the variables mentioned above, as



$$\omega_1 \mu_1 + \omega_2 \mu_2 = \sum_{i=1}^t i p_i + \sum_{i=t+1}^L i p_i = \mu_T \quad (3.4.9)$$

$$\omega_1 + \omega_2 = \sum_{i=1}^L p_i = 1 \quad (3.4.10)$$

The following presents the idea about discriminant criterion measures, which are used in a discriminant analysis to evaluate the optimal threshold at gray level t .

$$\sigma_w^2 + \sigma_b^2 = \sigma_T^2 \quad (3.4.11)$$

where

σ_w^2 : within-class variance of gray levels is defined as :

$$\sigma_w^2 = \omega_1 \sigma_1^2 + \omega_2 \sigma_2^2 \quad (3.4.12)$$

σ_B^2 : between-class variance of gray levels is defined as :

$$\sigma_B^2 = \omega_1(\mu_1 - \mu_T)^2 + \omega_2(\mu_2 - \mu_T)^2 = \omega_1\omega_2(\mu_2 - \mu_1)^2 \quad (3.4.13)$$

σ_T^2 : total variance of gray levels is defined as :

$$\sigma_T^2 = \sum_{i=1}^L (i - \mu_T)^2 p_i \quad (3.4.14)$$

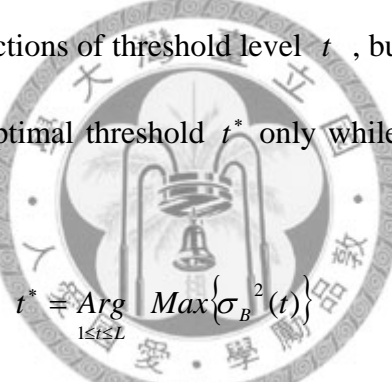
In the discriminant criterion, one would obtain optimal threshold at gray level t

while maximizing a σ_B^2/σ_W^2 ratio, which means maximize σ_B^2 and minimize σ_W^2 .

There is an example about optimal threshold shown in Fig 3.4.1.

σ_W^2 and σ_B^2 are functions of threshold level t , but σ_T^2 is independent of t .

It is equivalent to choose optimal threshold t^* only while the between-class variance σ_B^2 is maximized, that is



$$t^* = \underset{1 \leq t \leq L}{\operatorname{Arg}} \max \left\{ \sigma_B^2(t) \right\} \quad (3.4.15)$$

A threshold selection of t^* creates a binary image.

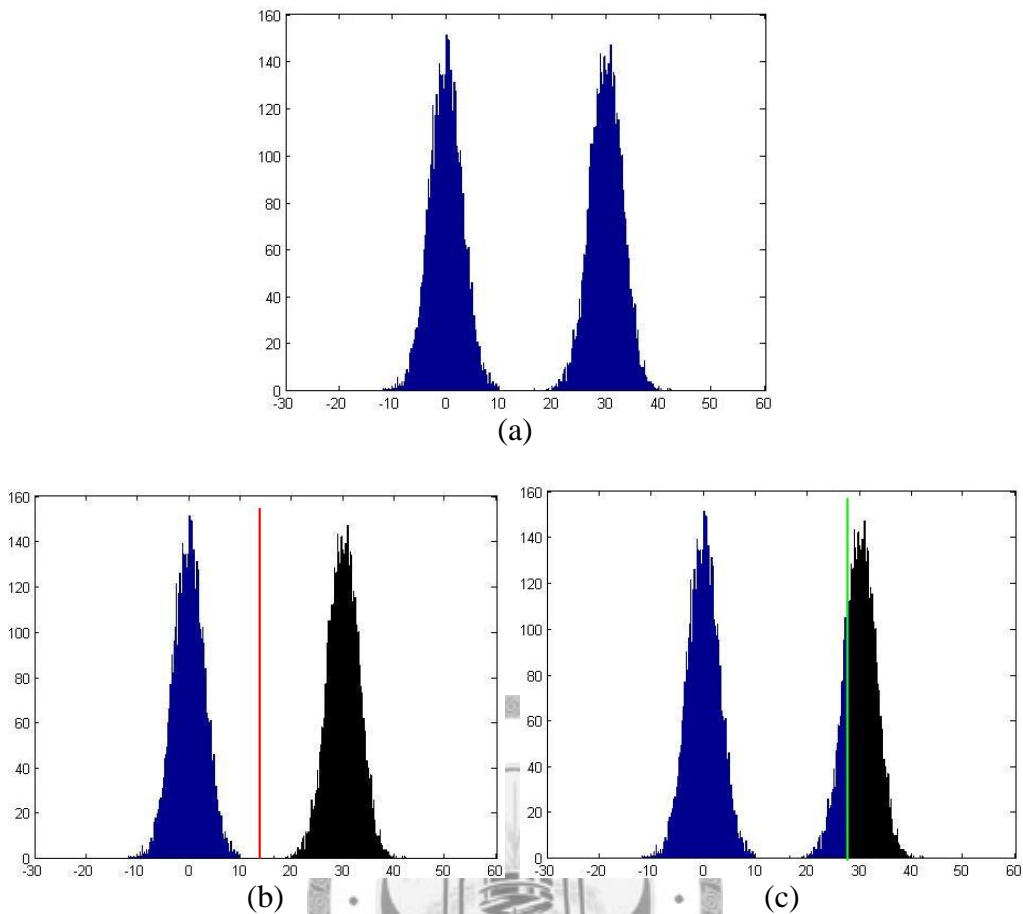


Fig 3.4.1 An example of the estimating optimal threshold selection dividing the distribution into two classes. (a) shows the original distribution. This algorithm proposes to computer the discriminant criterion function for any possible threshold, and chooses the optimal threshold according to the maximum ratio of a between-class variance and a within-class variance of the specific threshold. In (b) and (c), the red and green lines mean two possible thresholds, respectively. The blue part represents the first class and the black part represents the second class. In this example, it is clear that the (b) exhibits a better classified result than (c) dose, because (b) possesses the larger between-class variance and the smaller within-class variance than (c) does.

The concept mentioned above can be apt to extend to estimate multi-level thresholds in image processing [31]. Suppose that divide the pixels in an gray level image into M classes C_1, C_2, \dots, C_M with M-1 thresholds $\{t_1, t_2, \dots, t_{M-1}\}$:

For the first class C_1 : with gray levels $[1, \dots, t_1]$,

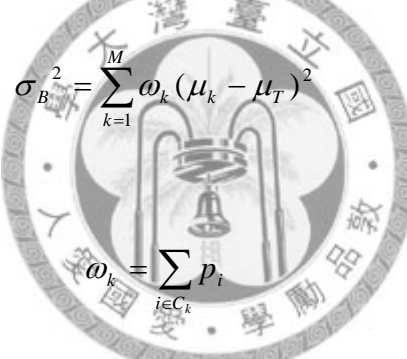
for the second class C_2 : with gray levels $[t_1 + 1, \dots, t_2]$, ...

for the i-th class C_i : with gray levels $[t_{i-1} + 1, \dots, t_i]$, ..., and

for the M-th class C_M : with gray levels $[t_{M-1} + 1, \dots, L]$

Maximize σ_B^2 to obtain the M-1optimal thresholds $\{t_1^*, t_2^*, \dots, t_{M-1}^*\}$.

$$\{t_1^*, t_2^*, \dots, t_{M-1}^*\} = \underset{1 \leq t_1 < \dots < t_{M-1} < L}{\operatorname{Arg}} \operatorname{Max}\{\sigma_B^2(t_1, t_2, \dots, t_{M-1})\} \quad (3.4.16)$$



$$\sigma_B^2 = \sum_{k=1}^M \omega_k (\mu_k - \mu_T)^2 \quad (3.4.17)$$

where

$$\omega_k = \sum_{i \in C_k} p_i \quad (3.4.18)$$

$$\mu_k = \sum_{i \in C_k} ip_i / \omega_k \quad (3.4.19)$$

The discriminant criterion proposed that maximizing the separability(a ratio of between-class variance and within-class variance) of each classes in the intensity function can obtain an optimal threshold. The method can also apply to multi-threshold selection problems as mentioned above.

In our case, the automatic thresholding selection is applied in many functions that are not only gray level of images but also intensity of feature or texture value to create distribution.

Chapter 4

Implementation and Results

This chapter provides the detailed procedure of the proposed approach step by step, and in order to demonstrate its performance, several examples considering different ultrasound images, containing cysts, benignant lesions, and/or malignant lesions are presented as well. MATLAB is chosen as a tool to implement our algorithm.



The general overview of methodology in this article is shown in Fig 4.1

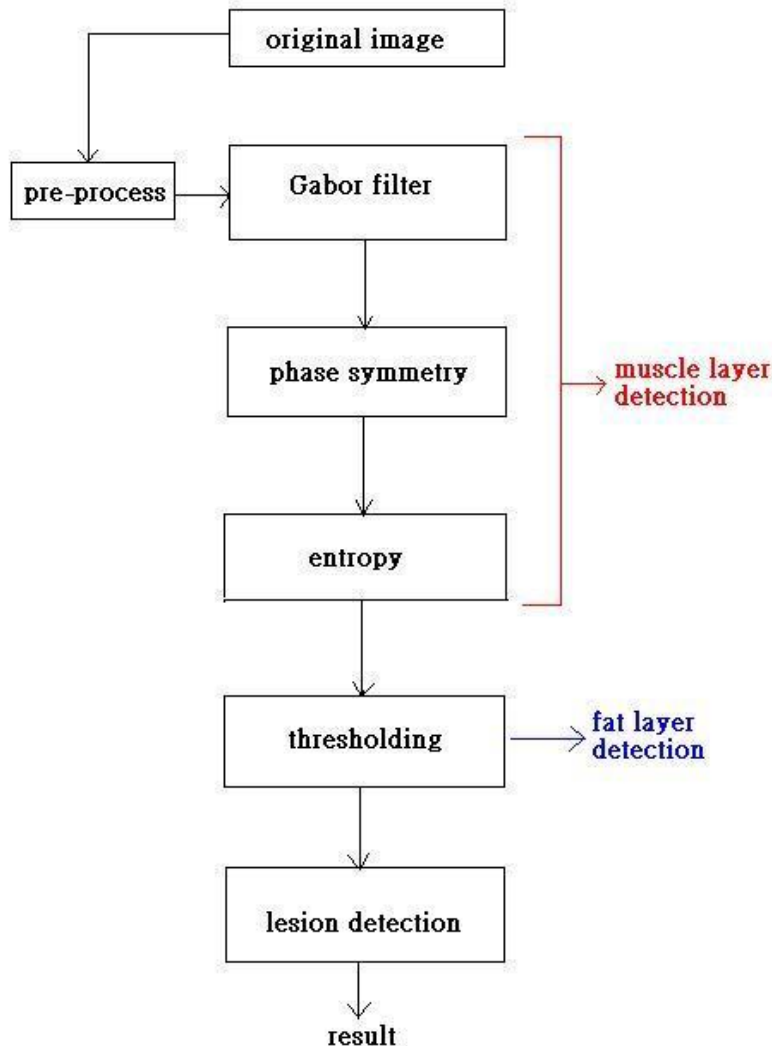


Fig 4.1 The flow char of the proposed algorithm is shown above. The original image is preprocessed and then processed by the Gabor filters and phase symmetry to derive PS map and to estimate entropy of normalized weighting angle distribution, identifying the area of muscle layer. Subsequently, the automatic thresholding selection and topological relation information approach are used to identify the area of the fat layer. Once the fat and muscle layers are determined, we use the in-between region (breast tissue) to detect lesions by investigating features of lesions, such as gray levels, region size, etc.

The basic idea of this article is to distinguish the fat layer, the breast tissue and the muscle layer in a single ultrasound breast image, and detect lesions only in the breast tissue to increase accuracy. The average processing time of total calculation for each 2-D ultrasound image was approximately 43 seconds on a personal computer, Athlon 64 X2 (2.71 GHz, 2GB of RAM).

The size of a Gaussian filter for preprocess was chosen 5 pixels and the standard deviation chosen 2 pixels smaller than the speckle size in order not to potentially obscure small lesions. Images thus were preprocessed to provide an input to the muscle layer detection technique.

I. Muscle layer detection :

In breast ultrasound images, the muscle layer is almost “rich horizontal strips” texture, which means an even symmetric characteristic for the human visual effect. As we mentioned before, we use the Gabor filters, phase symmetry and entropy to identify the region of the muscle layer.

a. Gabor filters :

In this article, we use even Gabor filters (i.e., pairs of symmetric Gaussian) and odd Gabor filters ((i.e., pairs of anti-symmetric Gaussian) to extract image features and define a phase symmetry indicator.

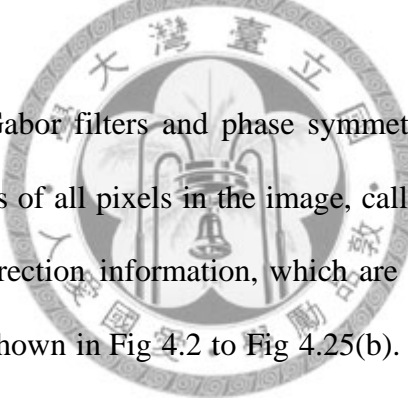
A set of two frequencies ($f = 2$) and four orientations ($N_\theta = 4$) pixels with the minimum filter wavelength $\lambda_{\min} = 25$ was used which provide good muscle layer localization in the presence of breast ultrasound images. B_f was set equal to 1 because several experiments have shown that the frequency bandwidth of the simple cells in the V1 area is about one octave [32]. $B_\theta = 180^\circ / N_\theta = 180^\circ / 4 = 45^\circ$

was chosen in this work.

Using the variables just mentioned, the horizontal pairs of different frequencies Gaussian filters can be derived. Then other pairs of Gaussian filters could be easily obtained by rotating the corresponding horizontal pairs. The DC component of each pair Gabor filter is set to equal zero.

b. Phase symmetry :

After the Gabor filters finish their calculations, the even and odd Gabor filters outputs can be derived by choosing a specific frequency and orientation. Each output as an indicator quantifies the phase symmetry property in the vicinity of each pixel; it means that it can derive local phase information (i.e., PS value) of each pixel from the image.



After using the Gabor filters and phase symmetry, we can obtain an image composed of PS values of all pixels in the image, called a PS map. PS maps offer more details of the direction information, which are not easily sensed by human visual. Examples are shown in Fig 4.2 to Fig 4.25(b). One can find out the muscle layer with clearer horizontal strips information.

c. Entropy :

Proceeded by a Sobel filter in the whole image to derive direction information of each pixel; each pixel of each region has its own magnitude and direction gradients. For each pixel of region in the PS map, summing the magnitude value of the all pixels in accordance with its angle degree can generate a weighting angle distribution, and the weighting angle distribution of each pattern is normalized by the sum of all magnitude of the pattern to compute the entropy in (3.3.2). The region size we use here is 32×32 .

If more points in a region have dissimilar direction, the entropy value is larger; if more points in a region have similar direction, the entropy value is smaller. The area of the muscle layer in the PS map has clear similar direction information, which is estimated from rich horizontal strips.

Herein, we can use entropy to identify whether the region has more points with similar direction information. In this article, in the PS map, we only consider the region whose entropy value is smaller.

Until this step, the area of the muscle layer in original image is identified. Some examples are shown in Fig 4.2 - 4.25(c). The red part shows the detected muscle layer region, the upper green line means the upper bound of the muscle layer, and the lower green line means the lower bound of the muscle layer.

Subsequently, eliminating the muscle layer region from original image leads that residual region of the original image can be thought as the fat layer and breast tissue.

II. Fat layer detection :

Here we use two features to identify a fat layer. One is smaller gray level value of which fat layer is displayed as dark regions; the other is that a fat layer is always in the top portion of the image. In this thesis, a gray level and topological information are used for an automatic thresholding technique to identify the fat layer in a single breast ultrasound image.

The results of I and II show that these two detection techniques may be served as the first step toward automatic lesion detection. Some examples are provided in Fig

4.2-4.25(d), and the green part that is upper than the top green line is the detected fat layer region.

After fat layer detection finishes, the residual region can be thought as the breast tissue only. It can reduce the false positive rate of lesion detection in breast tissue of the original ultrasound breast image.

III. Lesion detection :

Once the fat and muscle layers are determined, the hypoechoic regions in-between these two layers are more likely to be a breast lesion.

We use gray levels, height-width ratios, region sizes, and location information of lesions to detect lesions in-between region of the fat layer and muscle layer in the image. For example, the suspicious region near image boundary is not a lesion because of a low probability.

Fig 4.2-4.25(e) show the binary images of detected lesions upper than upper bound of the muscle layer. It detects the dark lesion as a lesion based on its gray level, height-width ratio, region size, and location information.

Fig 4.2-4.25(f) show that the regions of lesion ROI surrounded with the blue lines compare with radiologist outlines.

Fig 4.2-Fig 4.25 show the results of several examples of the overview of methodology applied to breast ultrasound images, and Fig 4.2 presents the example about a cyst.

Fig 4.3-Fig 4.8 present the examples of benign lesions.

Fig 4.9-Fig 4.21 present the examples of malignant lesions.

Fig 4.2-Fig.4.21 present the examples of successful lesion detections.

Fig 4.21-Fig.4.25 present the examples of unsuccessful lesion detection, including 3 benign lesion cases and one malignant lesion case.

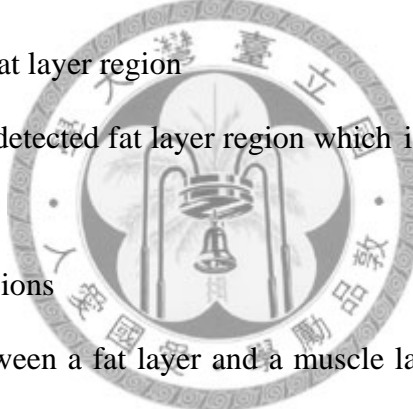
In each case, (a) to (b) mean that

- (a) Original image.
- (b) PS map.
- (c) Muscle layer region

The red part shows the detected muscle layer region. The upper green line means the upper bound of the muscle layer and the lower green line means the lower bound of the muscle layer. The region in-between the two green lines is the detected muscle layer.

- (d) Muscle layer region + fat layer region

The green part is the detected fat layer region which is upper than the upper green line.



- (e) Binary images show lesions

Use the region in-between a fat layer and a muscle layer to estimate lesion based on the gray level, region size and other information; the light means the detected lesion. The light region only shows the in-between fat layer and muscle layer.

- (f) Final result of lesion detection by our approach compare with radiologist outlines.

The blue rectangle region is identified as lesion by our approach and the region enclosed by the white contour is the lesion defined by a radiologist.

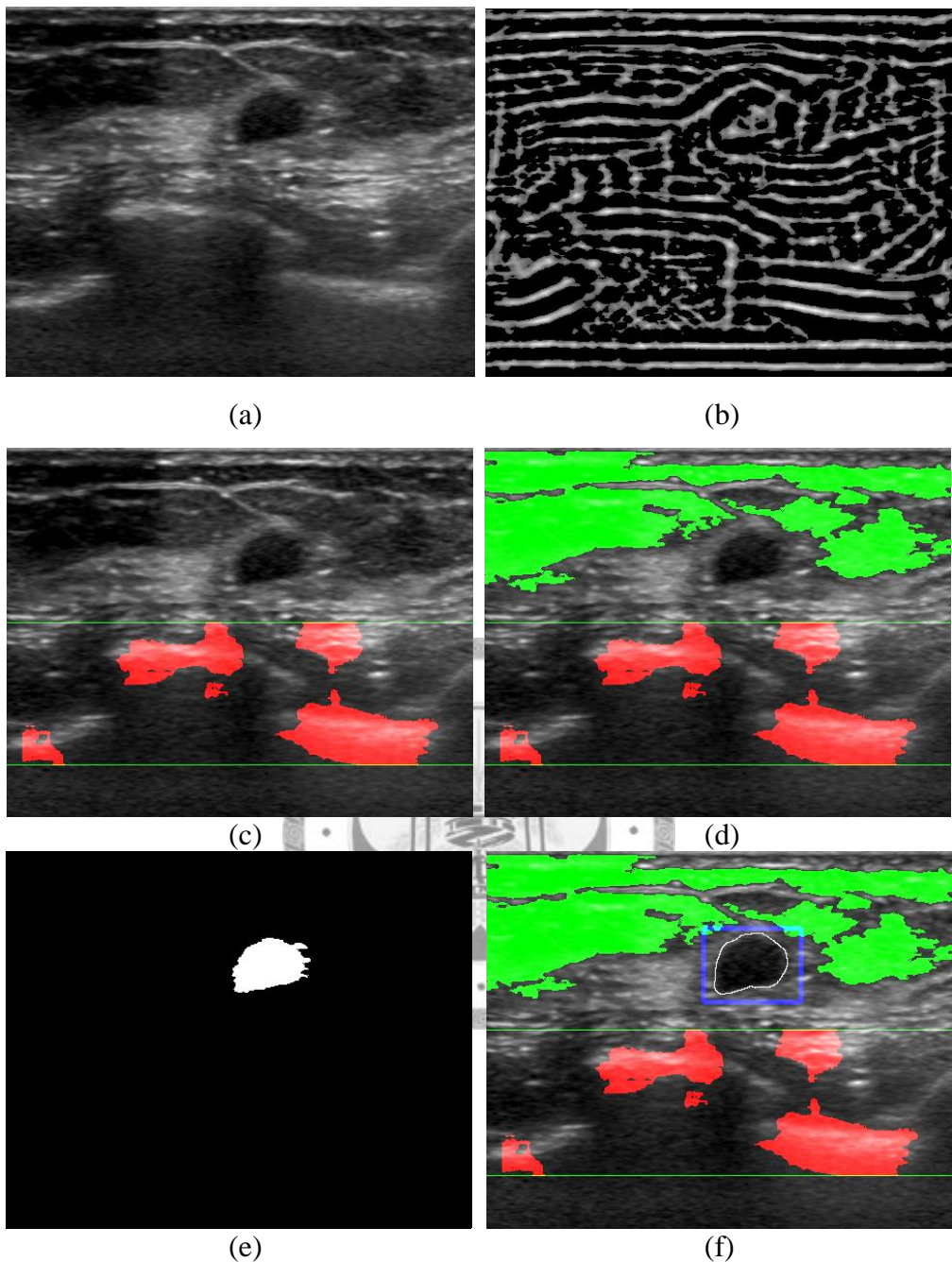


Fig 4.2 An example for cyst, in which cyst is identified, i.e. a true positive detection. (a) original image, (b) PS map, (c) the region in-between the two green lines is the detected muscle layer, (d) the green part is the detected fat layer region and (e) white part in binary image is the detected lesion. (f) final result of our approach, in which the cyst is detected by the blue rectangle and the region enclosed by the white contour is the lesion defined by a radiologist.

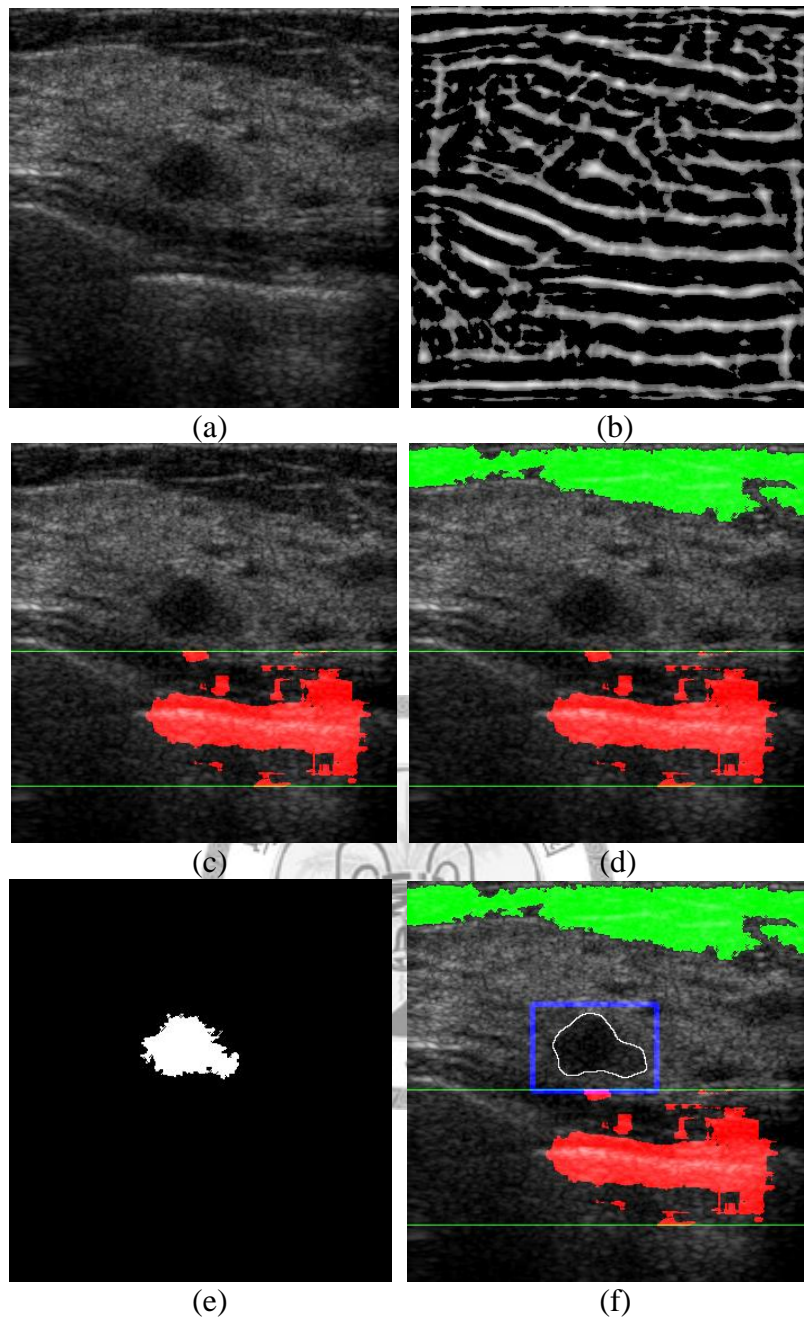


Fig 4.3 An example for simple benign lesion, in which lesion is identified. (a) original image, (b) PS map, (c) the region in-between the two green lines is the detected muscle layer, (d) the green part is the detected fat layer region and (e) the white part in binary image is the detected lesion. (f) the final result of our approach, in which the benign lesion is detected by the blue rectangle and the region enclosed by the white contour is the lesion defined by a radiologist.

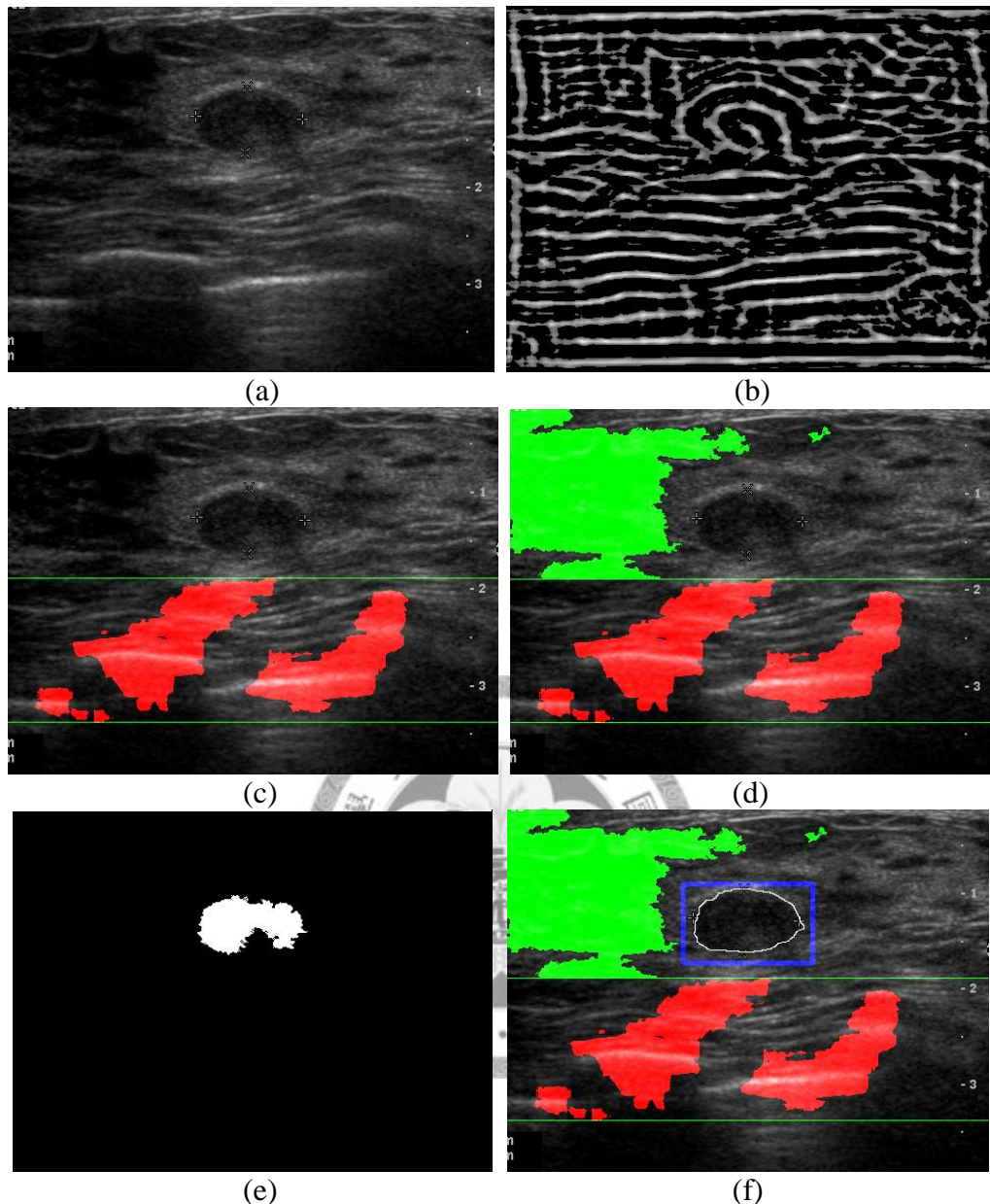


Fig 4.4 An example for benign lesion, in which the fat layer only appears left upper position in image. The benign lesion is identified, i.e. a true positive detection. (a) original image, (b) PS map, (c) the region in-between the two green lines is the detected muscle layer, (d) the green part is the detected fat layer region and (e) the white part in binary image is the detected lesion. (f) the final result of our approach, in which the benign lesion is detected by the blue rectangle and the region enclosed by the white contour is the lesion defined by a radiologist.

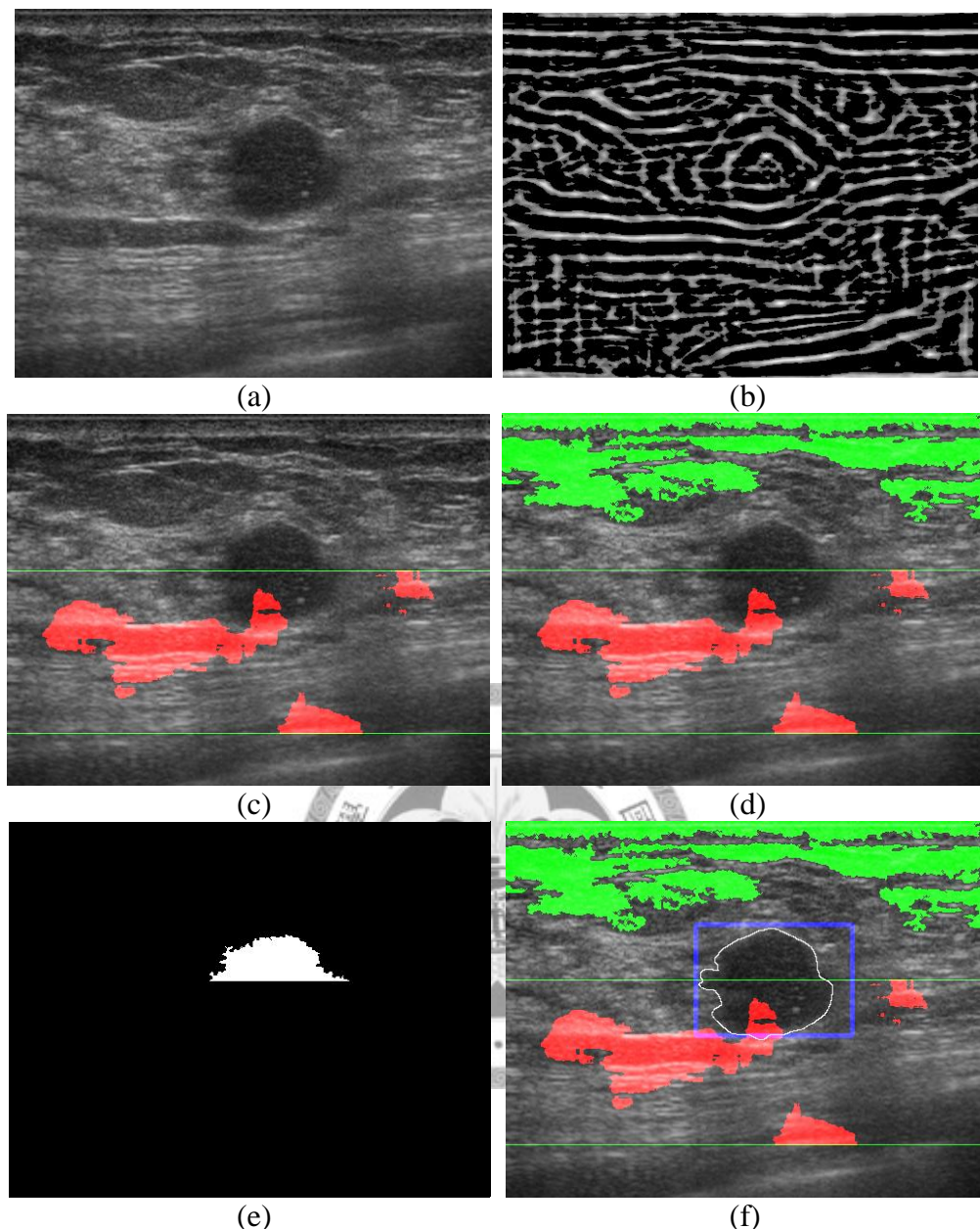


Fig 4.5 An example for benign lesion, in which one part of the lesion appears lower than the detected muscle layer upper bound. In this case, it is clear that the method we proposed can also identify the part of lesion lower than muscle layer upper bound. (a) original image, (b) PS map, (c) the region in-between the two green lines is the detected muscle layer, (d) the green part is the detected fat layer region, (e) the white part in binary image is the detected lesion. (f) the blue rectangle shows our result and radiologist outline is depicted with white contour.

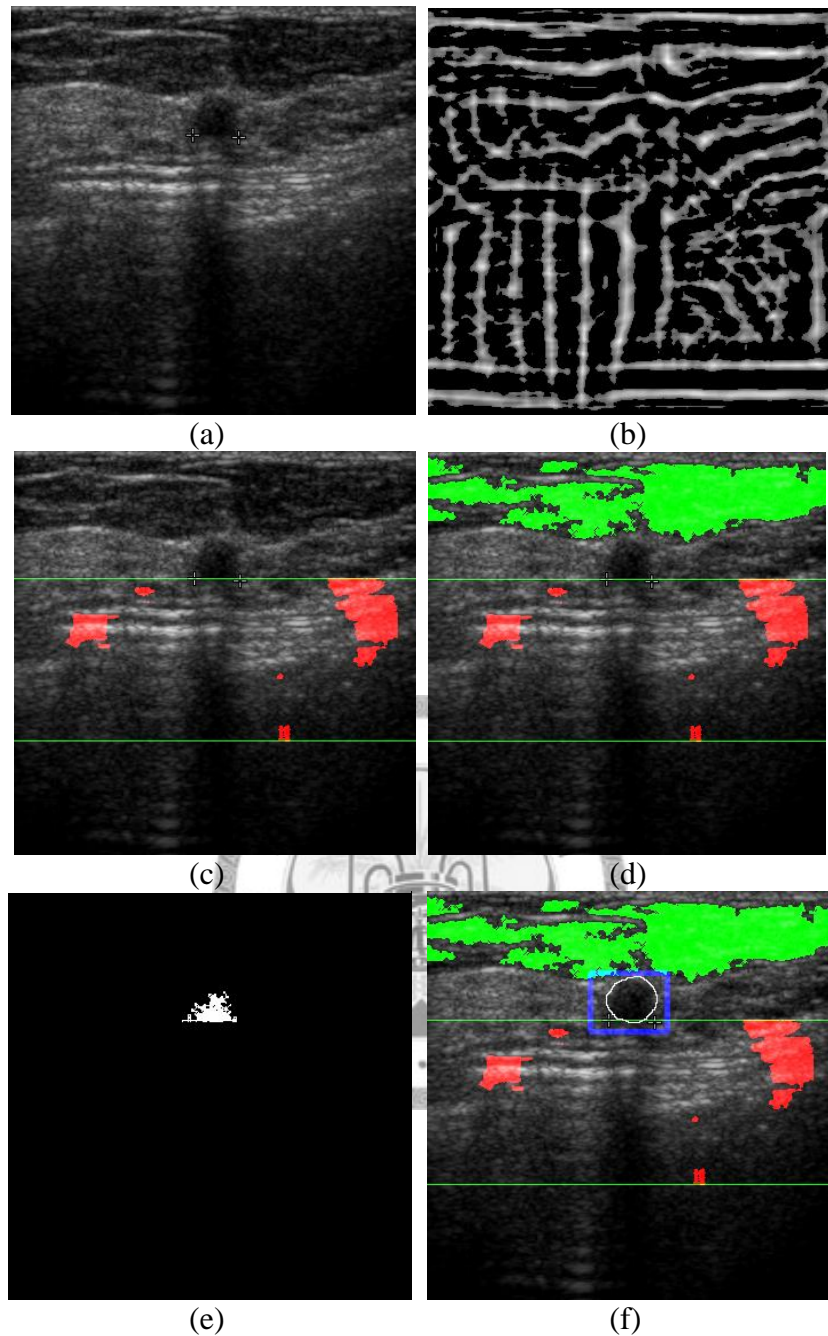


Fig 4.6 An example for benign lesion, in which the size of the lesion is small. (a) original image, **(b)** PS map, **(c)** the region in-between the two green lines is the detected muscle layer, **(d)** the green part is the detected fat layer region and **(e)** the white part in binary image is the detected lesion. **(f)** the final result of our approach, in which the benign lesion is detected by the blue rectangle and the region enclosed by the white contour is the lesion defined by a radiologist.

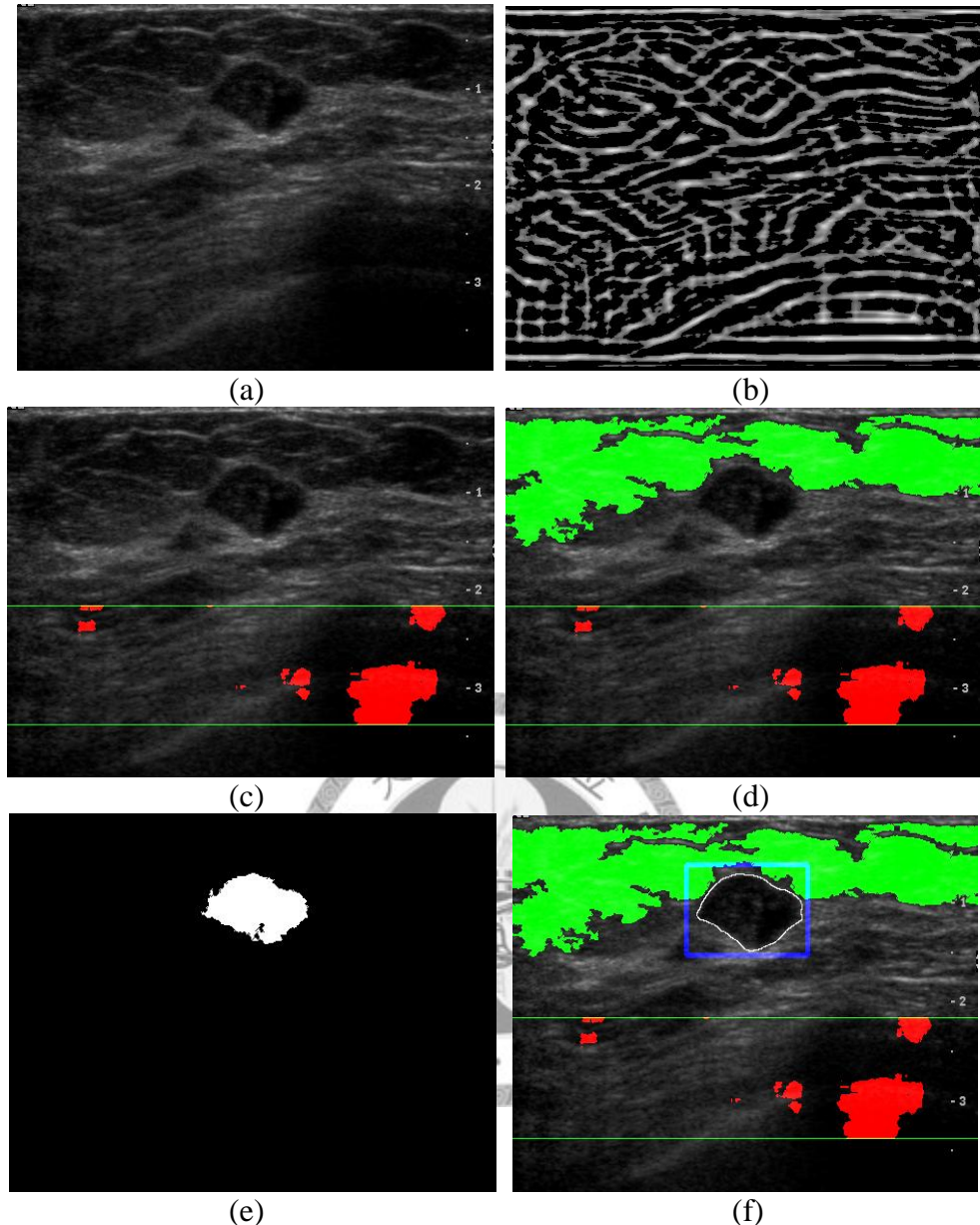


Fig 4.7 An example for benign lesion, in which the fat layer is near to the lesion, and the muscle layer is not horizontal strips. (a) original image, (b) PS map, (c) the region in-between the two green lines is the detected muscle layer, (d) the green part is the detected fat layer region and (e) the white part in binary image is the detected lesion. (f) the final result of our approach, in which the benign lesion is detected by the blue rectangle and the region enclosed by the white contour is the lesion defined by a radiologist.

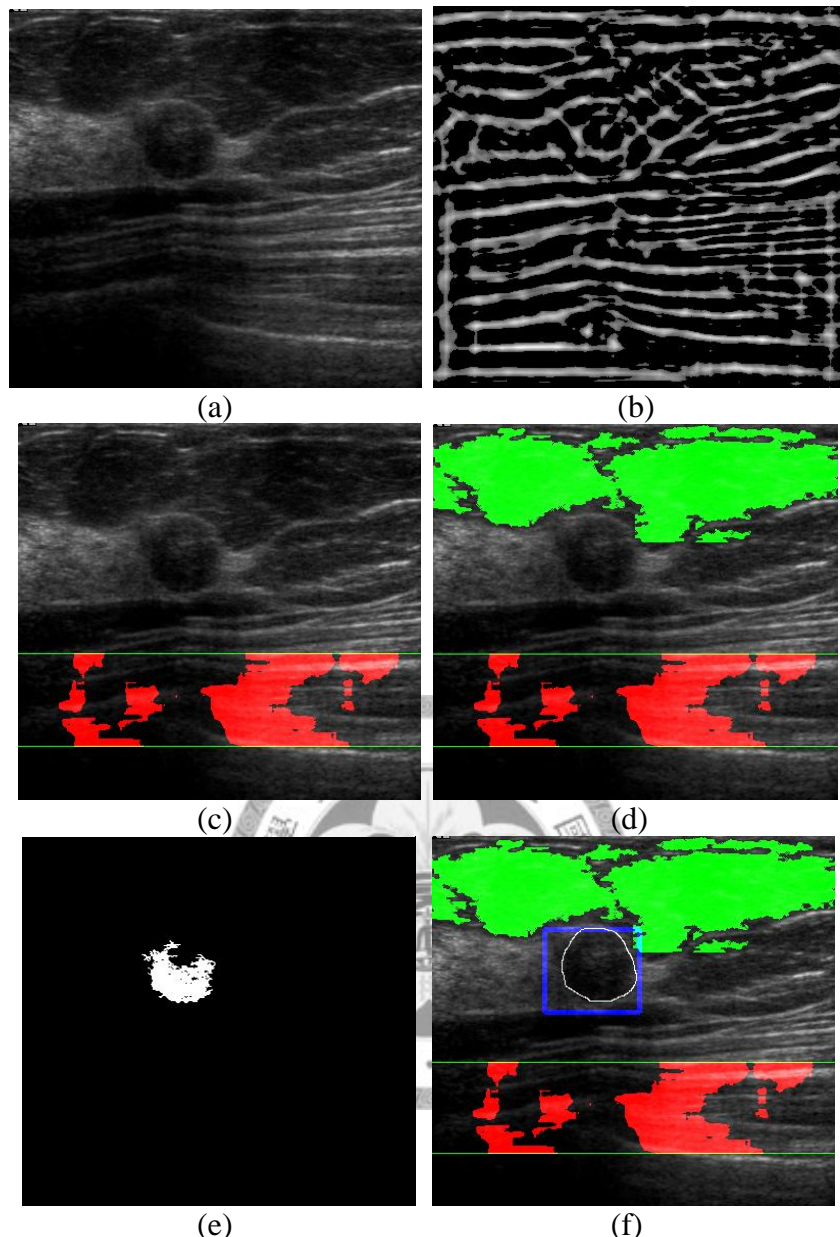


Fig 4.8 An example for benign lesion, in which the fat layer is near to the lesion and the artifact appears on the muscle layer. (a) original image, (b) PS map, (c) the region in-between the two green lines is the detected muscle layer, (d) the green part is the detected fat layer region and (e) the white part in binary image is the detected lesion. (f) the final result of our approach, in which the benign lesion is detected by the blue rectangle and the region enclosed by the white contour is the lesion defined by a radiologist.

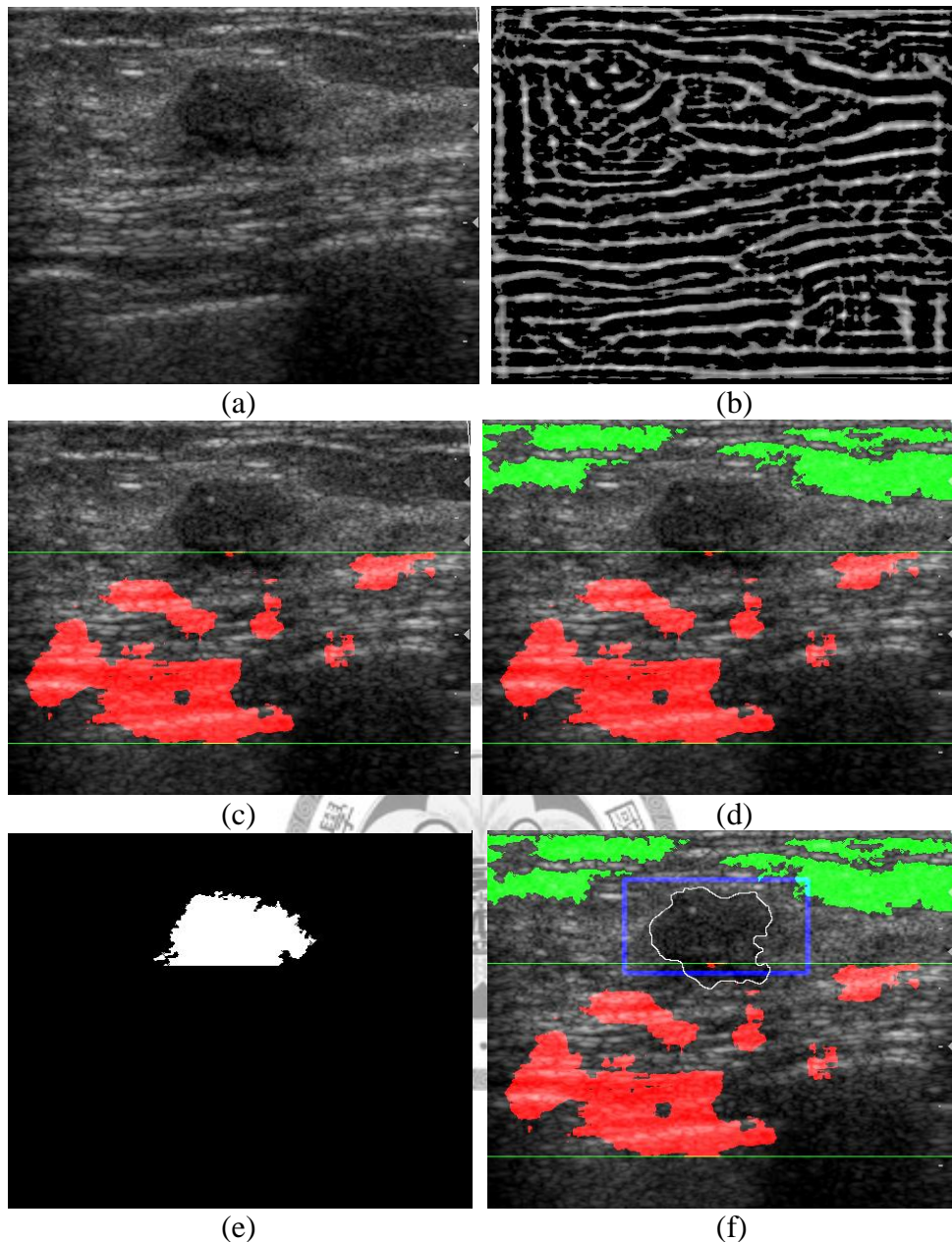


Fig 4.9 An example for simple malignant lesion, in which the texture of the fat and muscle layers are obvious. (a) original image, (b) PS map, (c) the region in-between the two green lines is the detected muscle layer, (d) the green part is the detected fat layer region and(e) the white part in binary image is the detected lesion. (f) the final result of our approach, in which the malignant lesion is detected by blue rectangle and the region enclosed by the white contour is the lesion defined by a radiologist.

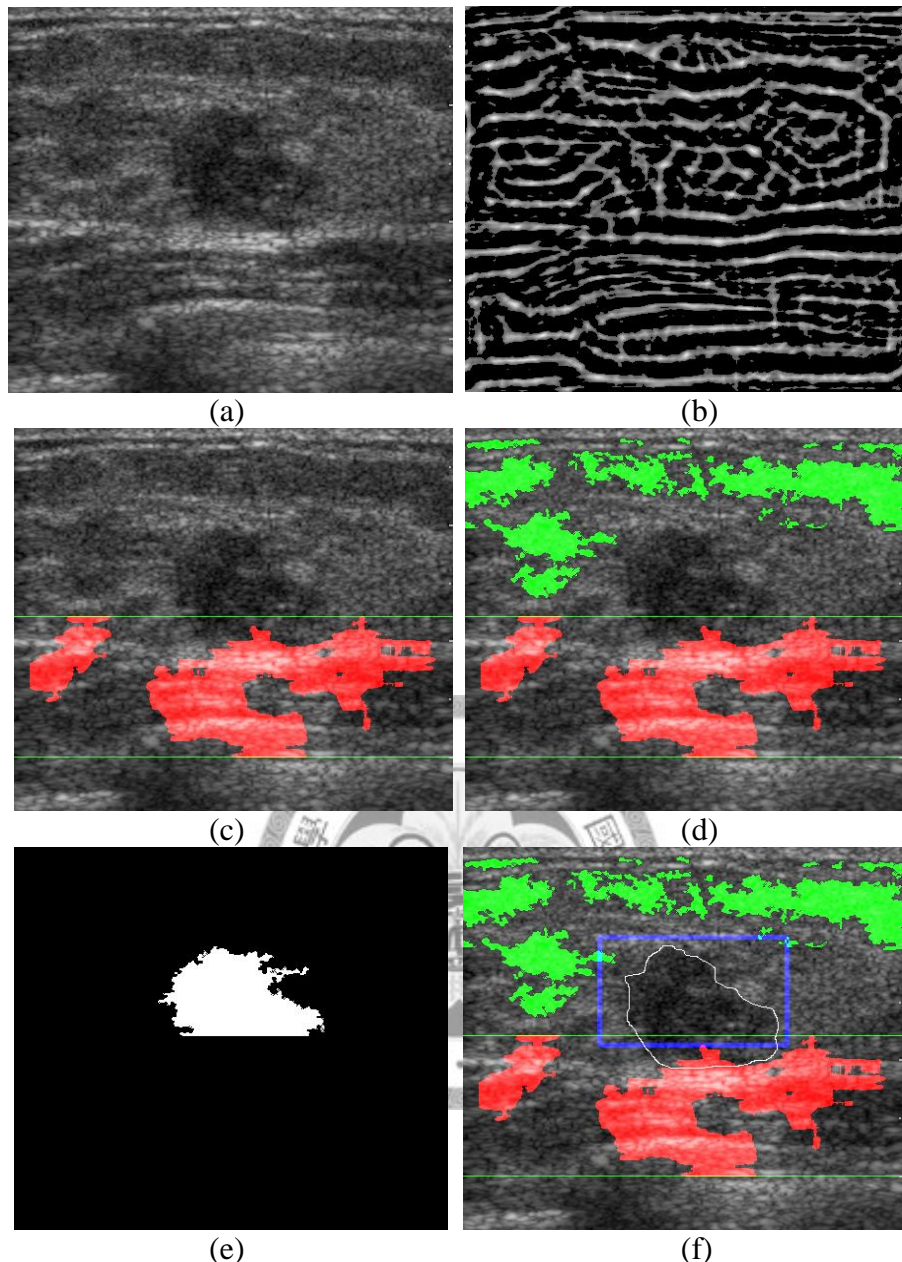


Fig 4.10 An example for simple malignant lesion, in which the muscle layer appears obvious. (a) original image, (b) PS map, (c) the region in-between the two green lines is the detected muscle layer, (d) the green part is the detected fat layer region and (e) the white part in binary image is the detected lesion. (f) the final result of our approach, in which the malignant lesion is detected by the blue rectangle and the region enclosed by the white contour is the lesion defined by a radiologist.

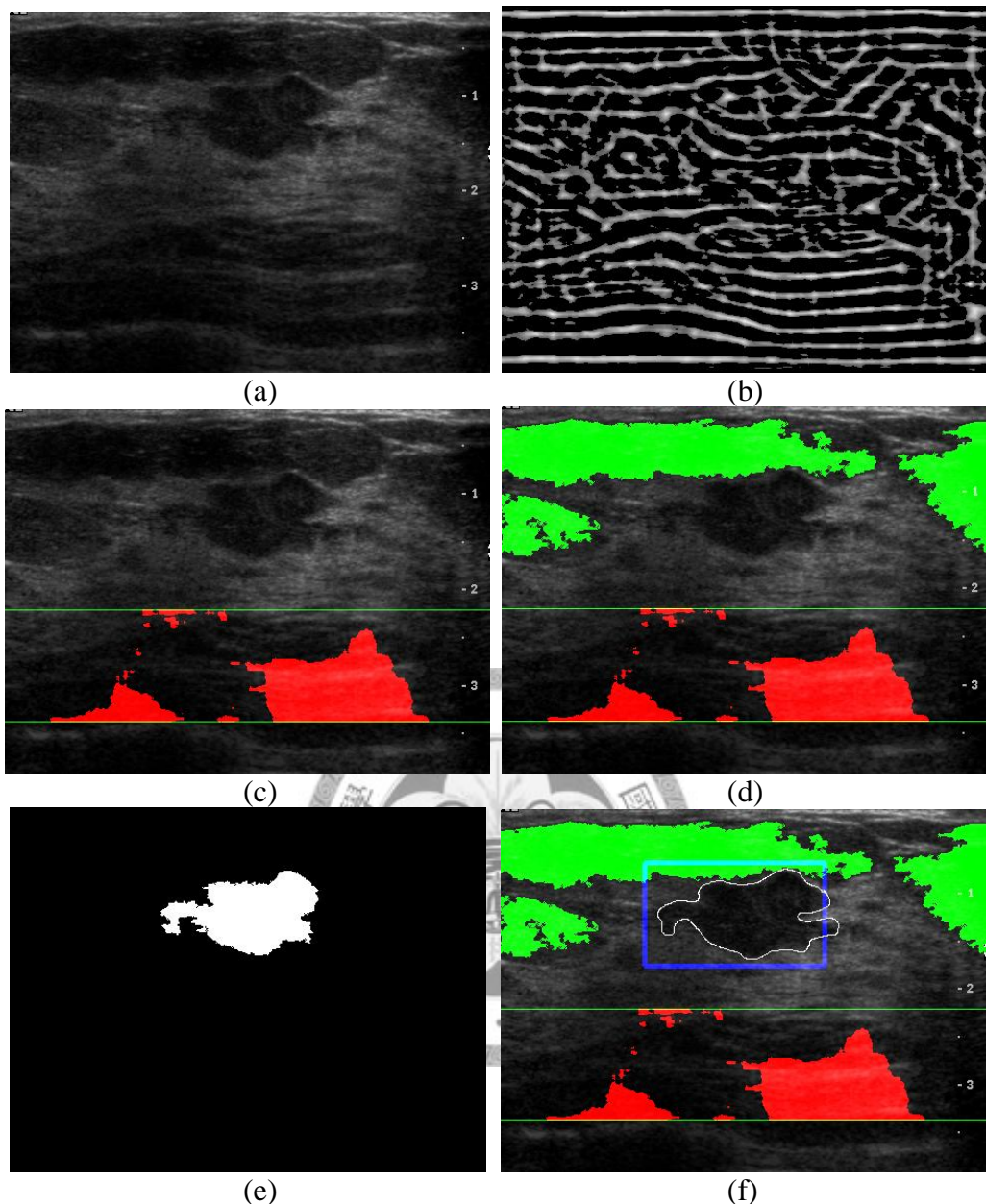


Fig 4.11 An example for malignant lesion, in which the fat layer is near to the lesion and the muscle layer is not obvious. (a) original image, (b) PS map, (c) the region in-between the two green lines is the detected muscle layer, (d) the green part is the detected fat layer region and (e) white part in binary image is the detected lesion. (f) the final result of our approach, in which the malignant lesion is detected by the blue rectangle and the region enclosed by the white contour is the lesion defined by a radiologist.

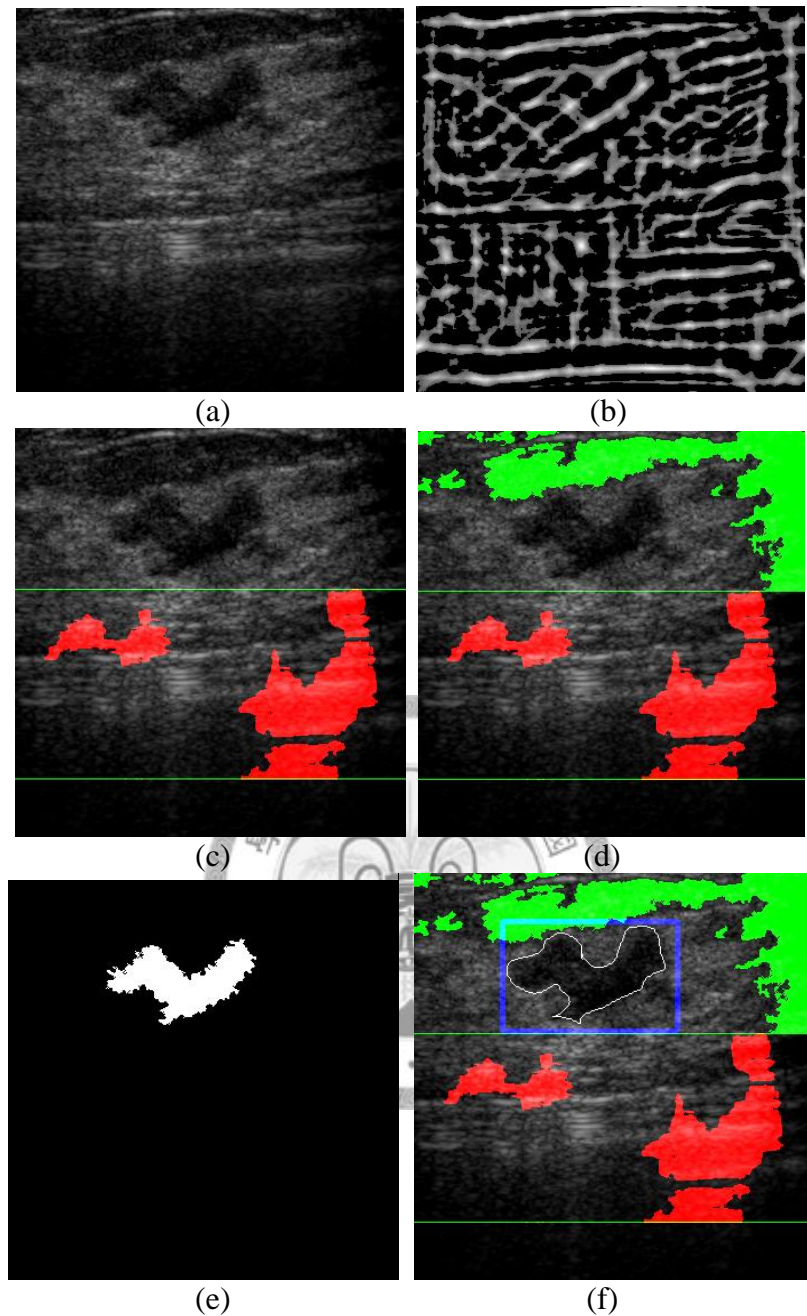


Fig 4.12 An example for malignant lesion, in which the shape of the lesion is irregular, and the texture of muscle layer is not obvious. (a) original image, (b) PS map, (c) the region in-between the two green lines is the detected muscle layer, (d) the green part is the detected fat layer region and (e) the white part in binary image is the detected lesion. (f) the blue rectangle shows the result by our approach and radiologist outline is depicted with white contour.

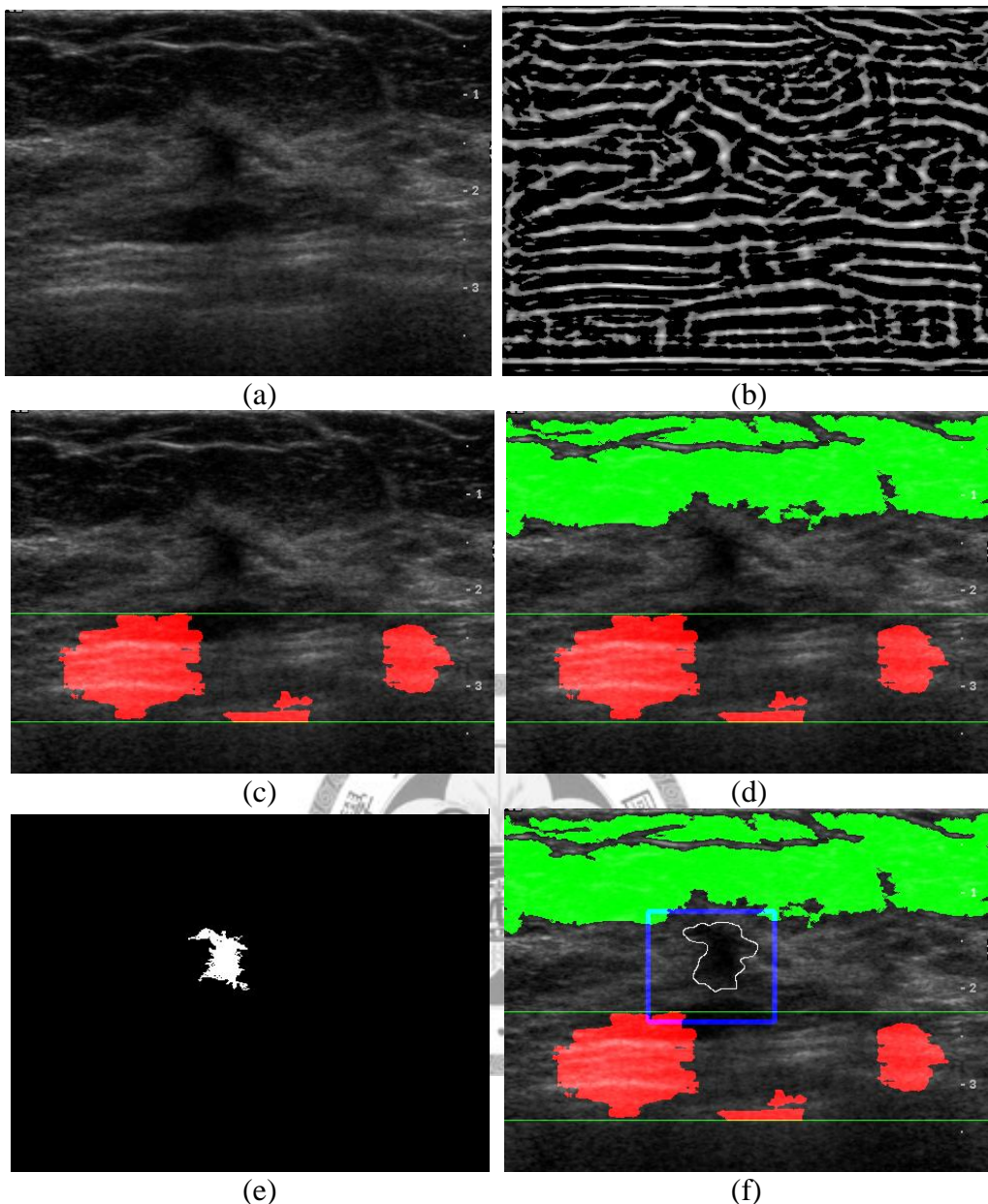


Fig 4.13 An example for malignant lesion, in which the shape of the lesion is irregular, and the muscle layer appears blurring. (a) original image, (b) PS map, (c) the region in-between the two green lines is the detected muscle layer, (d) the green part is the detected fat layer region and (e) the white part in binary image is the detected lesion. (f) the final result of our approach, in which the malignant lesion is detected by the blue rectangle and the region enclosed by the white contour is the lesion defined by a radiologist.

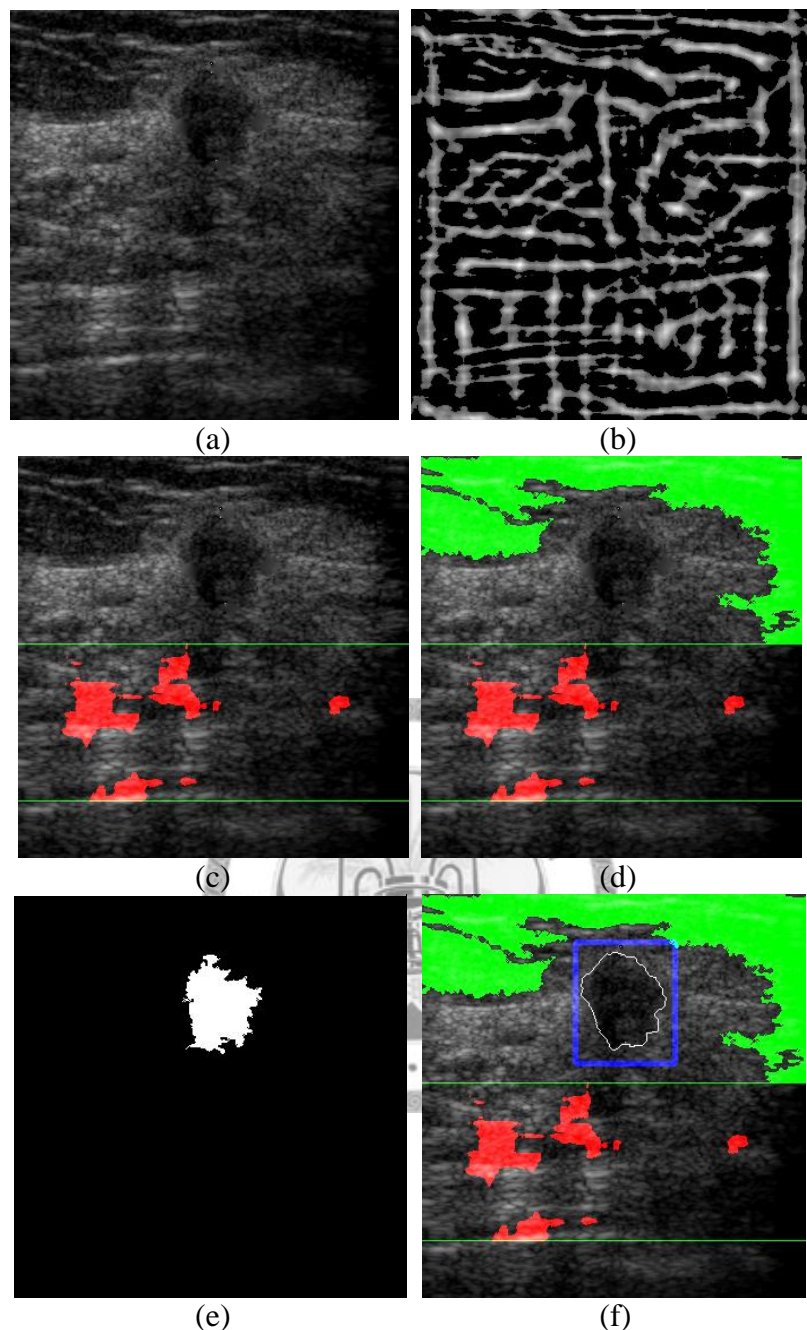


Fig 4.14 An example for malignant lesion, in which the right part of the muscle layer is blurred by artifacts. (a) original image, (b) PS map, (c) the region in-between the two green lines is the detected muscle layer, (d) the green part is the detected fat layer region and (e) the white part in binary image is the detected lesion.(f) the blue rectangle shows the result by our approach and radiologist outline is depicted with white contour.

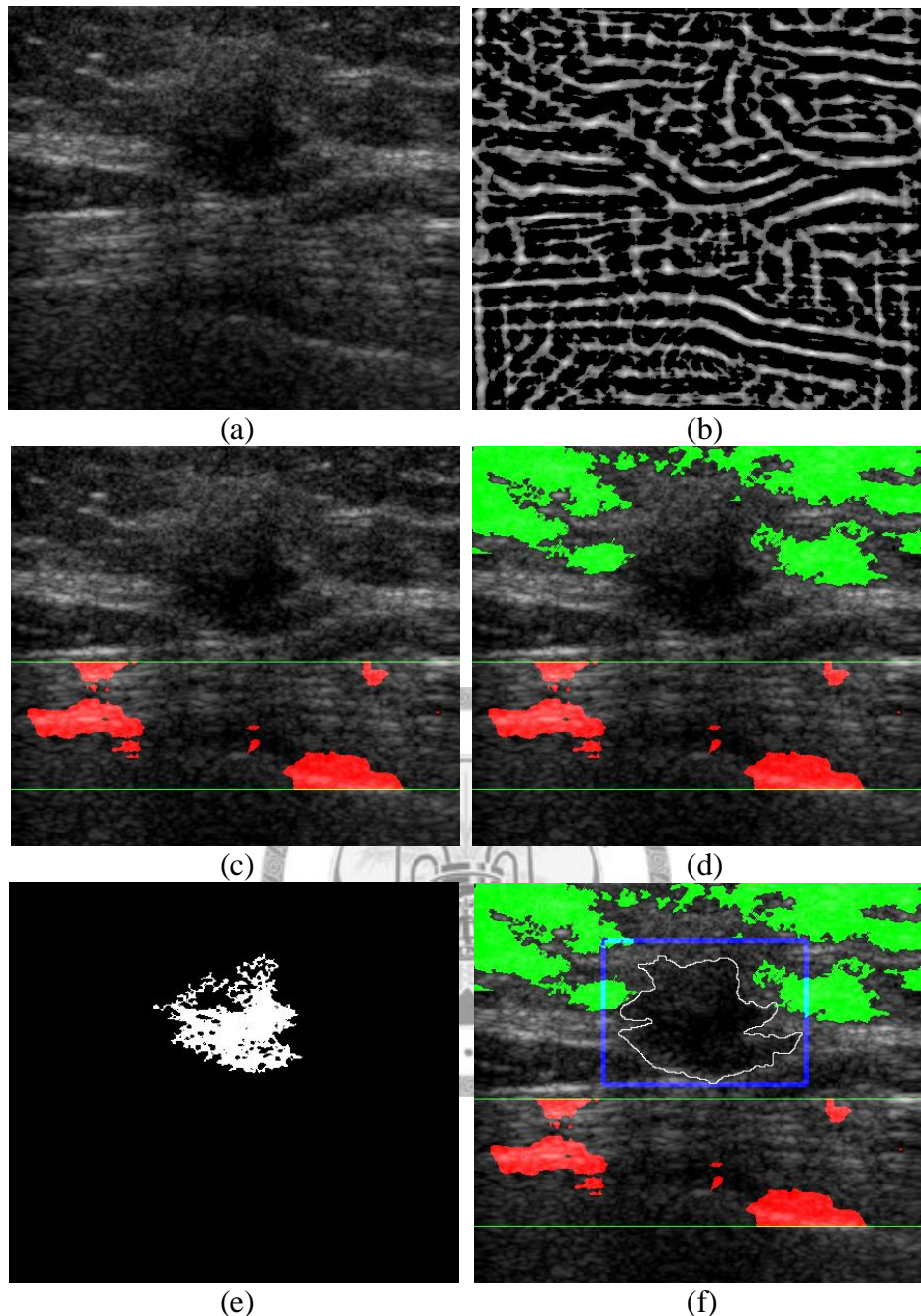


Fig 4.15 An example for malignant lesion, in which the shape of the lesion is irregular, and the artifacts appear on the muscle layer. (a) original image, (b) PS map, (c) the region in-between the two green lines is the detected muscle layer, (d) the green part is the detected fat layer region and (e) the white part in binary image is the detected lesion. (f) the blue rectangle shows the result by our approach and radiologist outline is depicted with white contour.

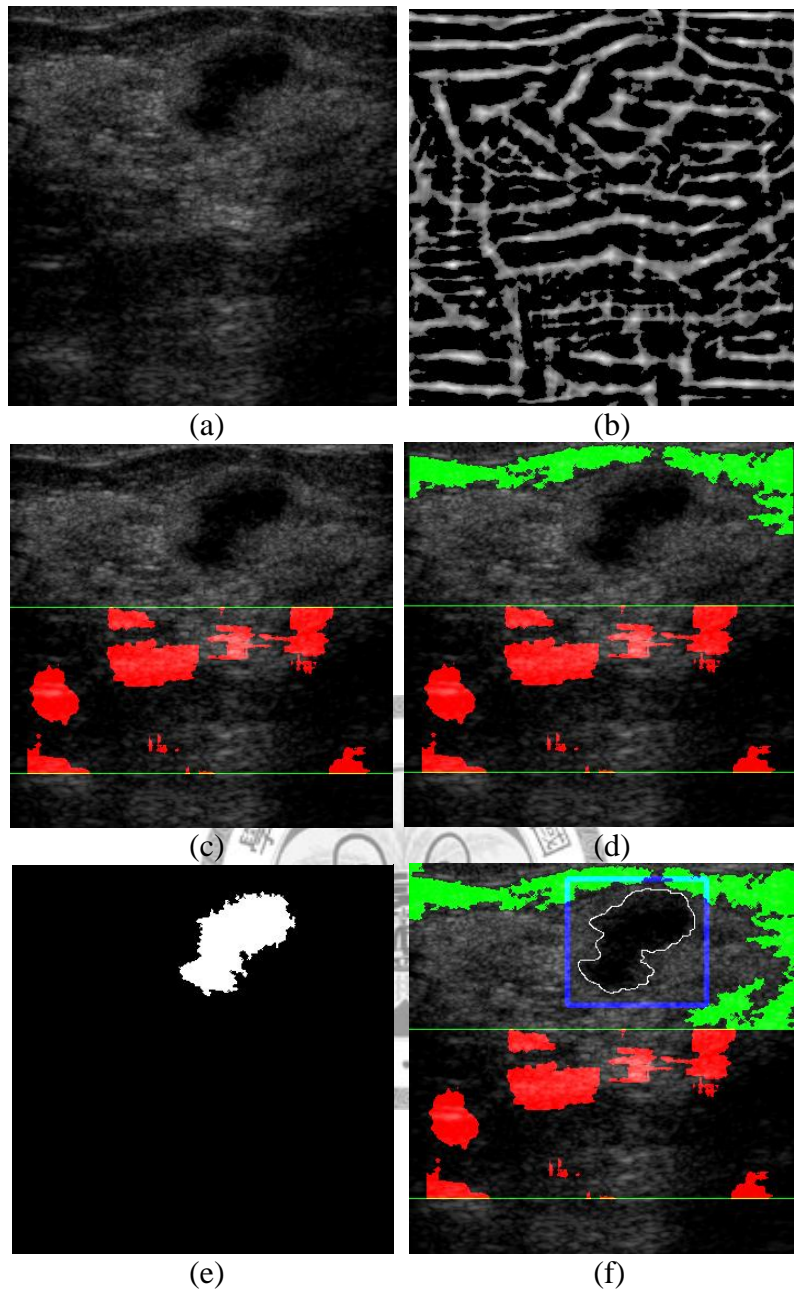


Fig 4.16 An example for malignant lesion, in which the fat layer is near to the lesion and the artifacts appear on the muscle layer. (a) original image, (b) PS map, (c) the region in-between the two green lines is the detected muscle layer, (d) the green part is the detected fat layer region and (e) the white part in binary image is the detected lesion. (f) the blue rectangle shows the result by our approach and radiologist outline is depicted with white contour.

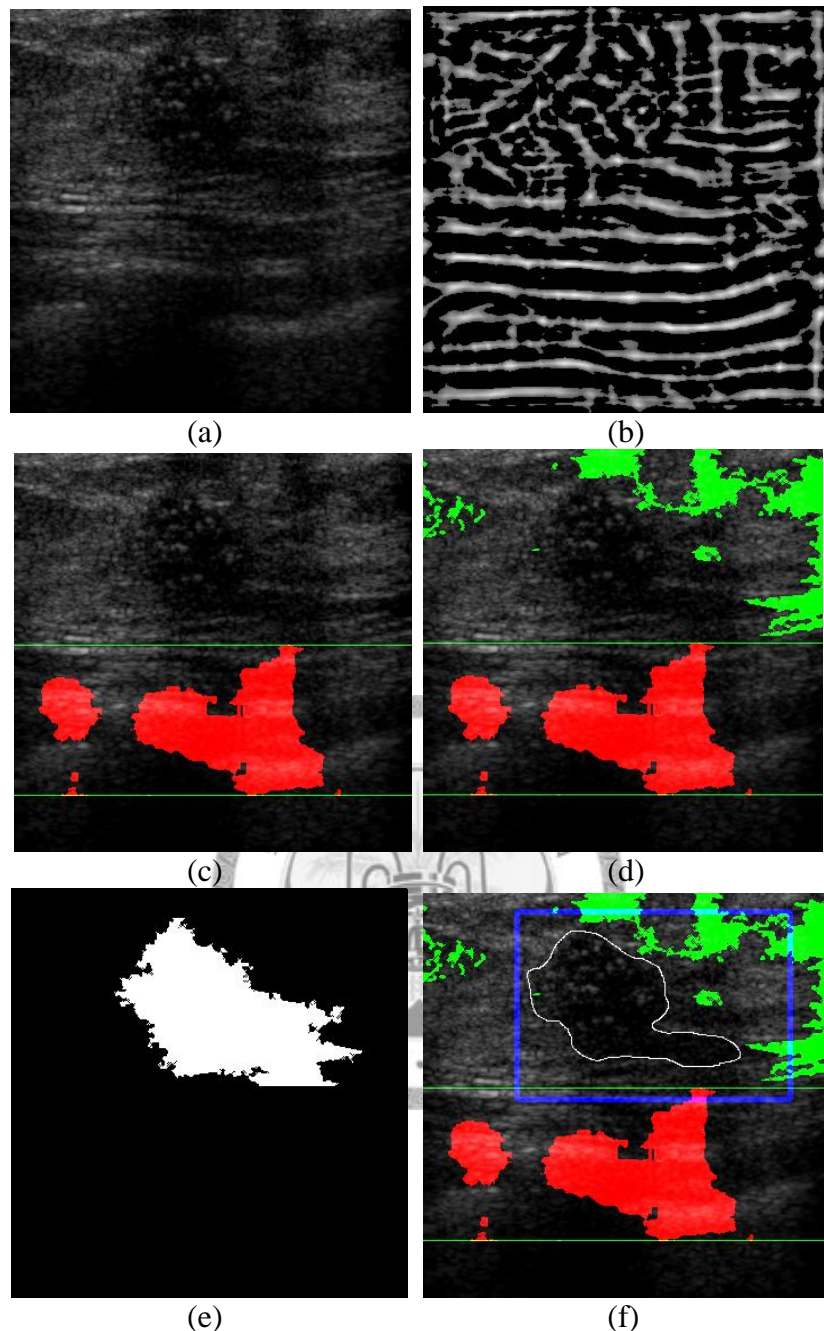


Fig 4.17 An example for malignant lesion, in which the fat layer appears blurring and the shadowing effect appears on the muscle layer. (a) original image, (b) PS map, (c) the region in-between the two green lines is the detected muscle layer, (d) the green part is the detected fat layer region and (e) white part in binary image is the detected lesion. (f) the blue rectangle shows the result by our approach and radiologist outline is depicted with white contour.

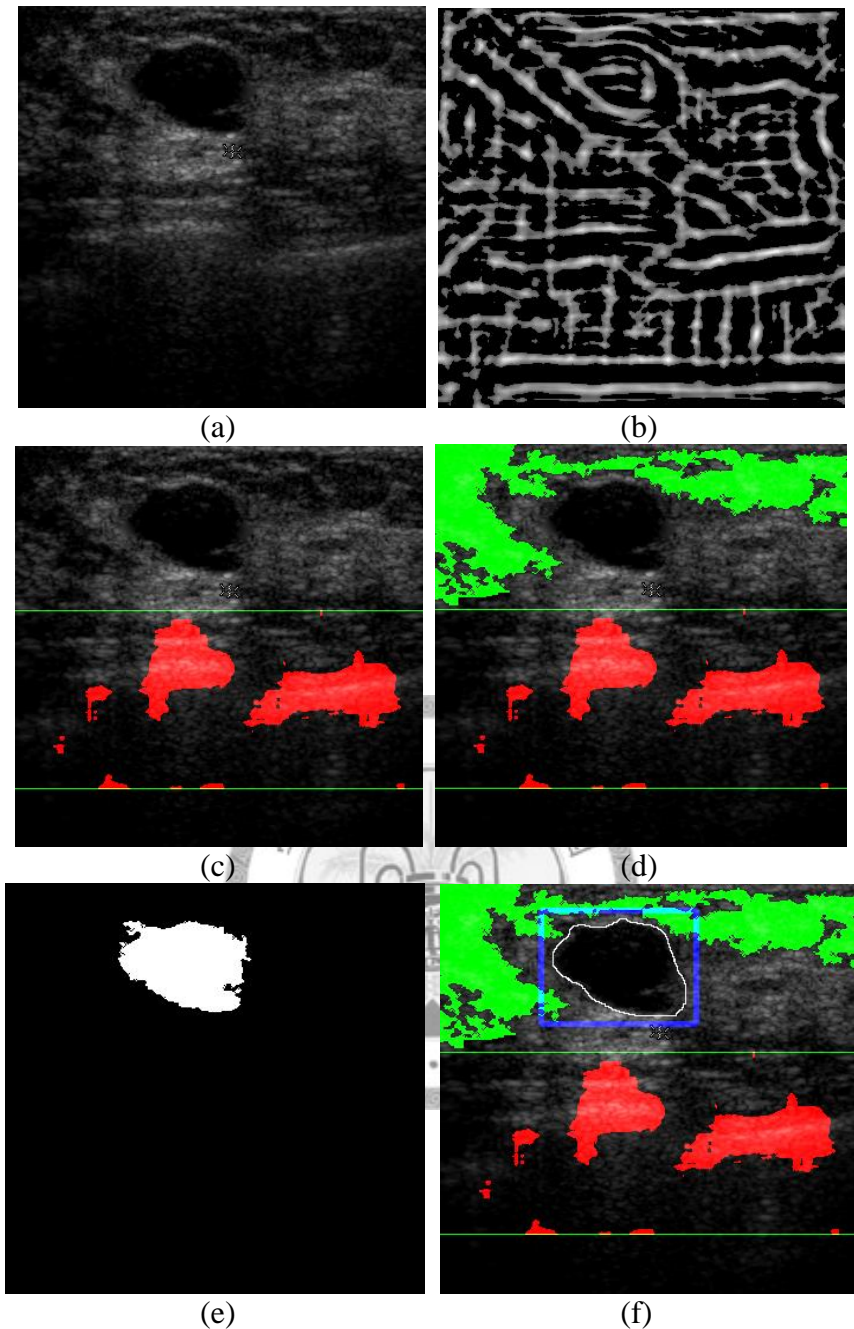


Fig 4.18 An example for malignant lesion, in which the fat layer is near to the lesion and the artifacts effect appear on the muscle layer. (a) original image, (b) PS map, (c) the region in-between the two green lines is the detected muscle layer, (d) the green part is the detected fat layer region and (e) the white part in binary image is the detected lesion. (f) the blue rectangle shows the result by our approach and radiologist outline is depicted with white contour.

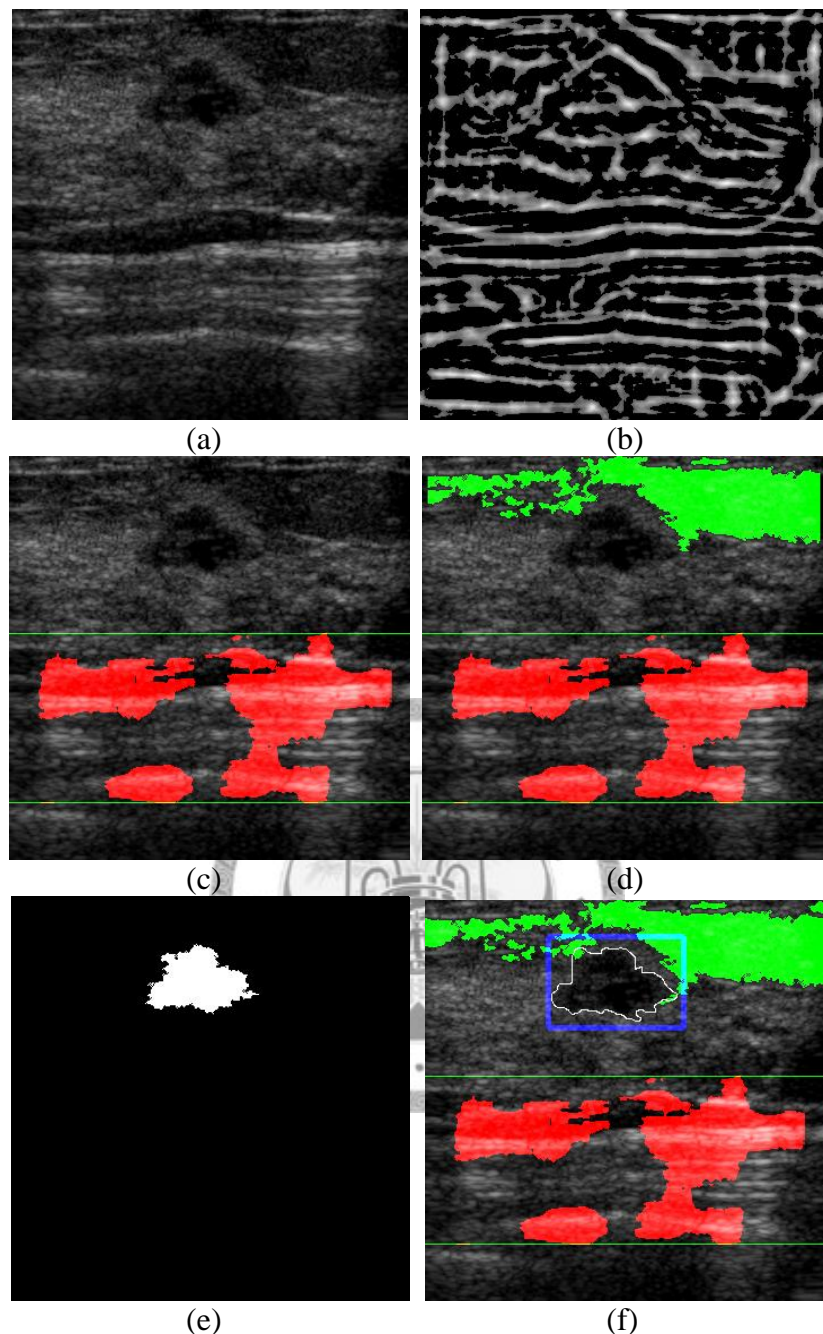


Fig 4.19 An example for malignant lesion, in which the fat layer is near to the lesion and the texture of muscle layer is obvious. (a) original image, (b) PS map, (c) the region in-between the two green lines is the detected muscle layer, (d) the green part is the detected fat layer region and (e) the white part in binary image is the detected lesion. (f) the blue rectangle shows the result by our approach and radiologist outline is depicted with white contour.

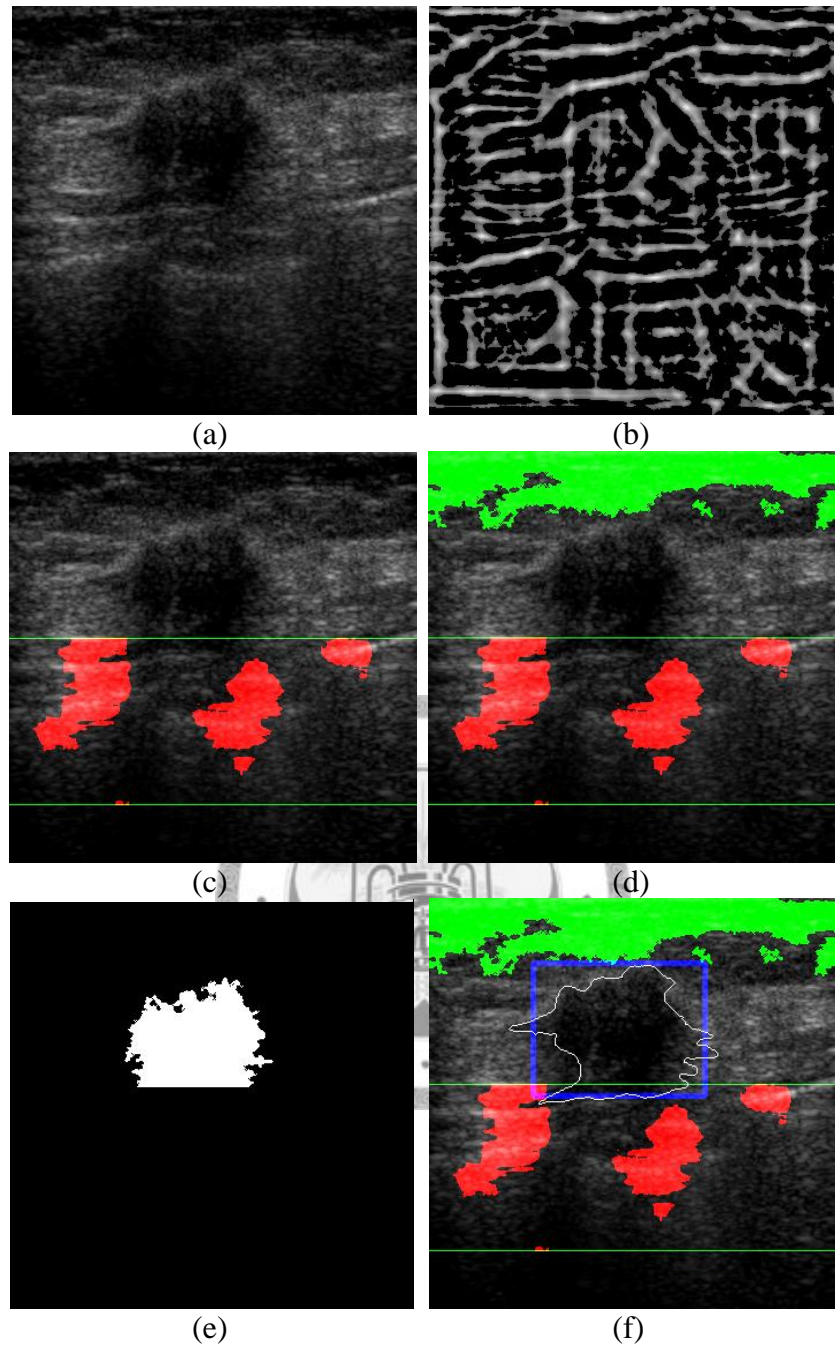


Fig 4.20 An example for malignant lesion, in which the shadowing effect appears on the muscle layer. (a) original image, (b) PS map, (c) the region in-between the two green lines is the detected muscle layer, (d) the green part is the detected fat layer region and (e) the white part in binary image is the detected lesion. (f) the blue rectangle shows the result by our approach and radiologist outline is depicted with white contour.

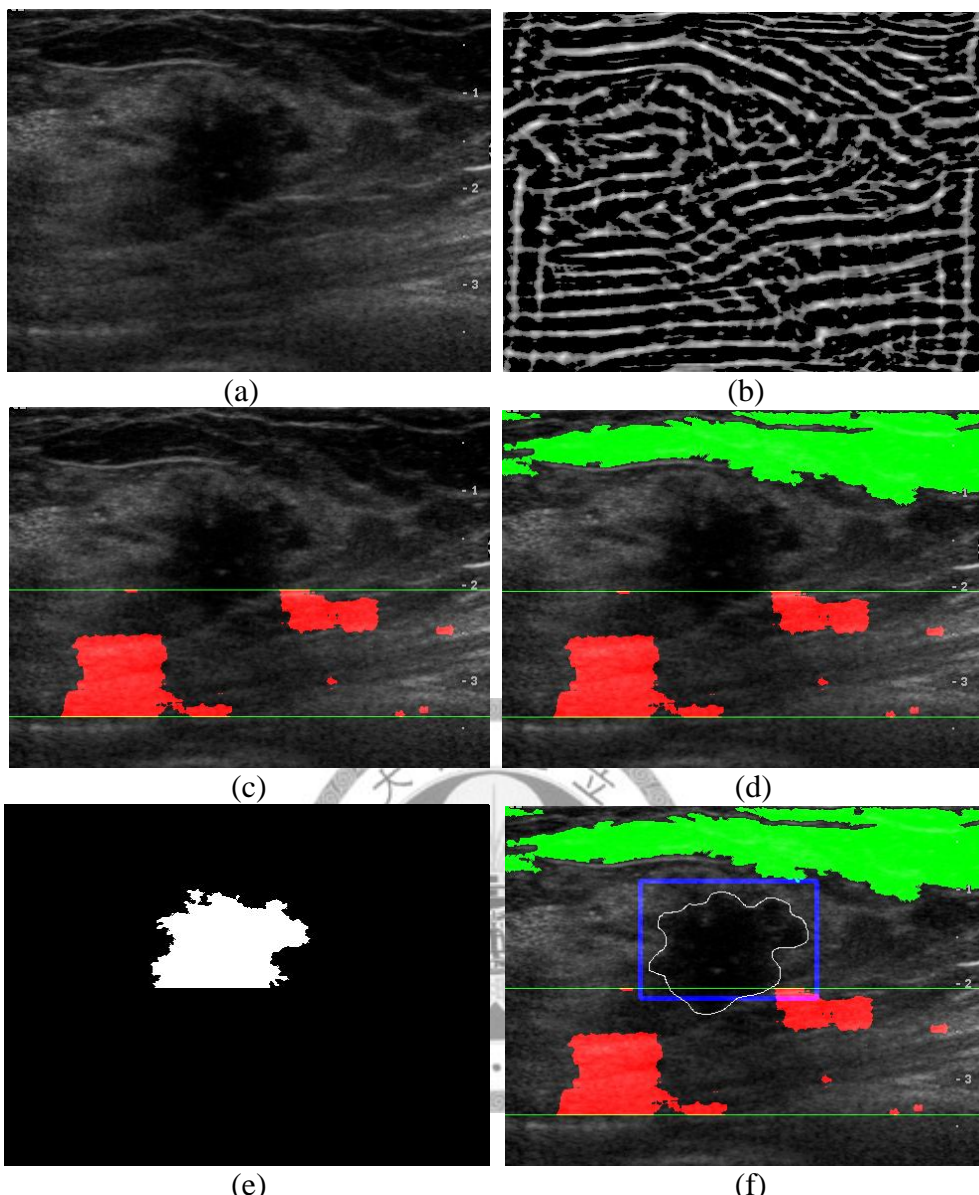


Fig 4.21 An example for malignant lesion, in which the shape of the lesion is irregular and the shadowing effect appears on the muscle layer. (a) original image, (b) PS map, (c) the region in-between the two green lines is the detected muscle layer, (d) the green part is the detected fat layer region and (e) the white part in binary image is the detected lesion. (f) the final result of our approach, in which the malignant lesion is detected by the blue rectangle and the region enclosed by the white contour is the lesion defined by a radiologist.

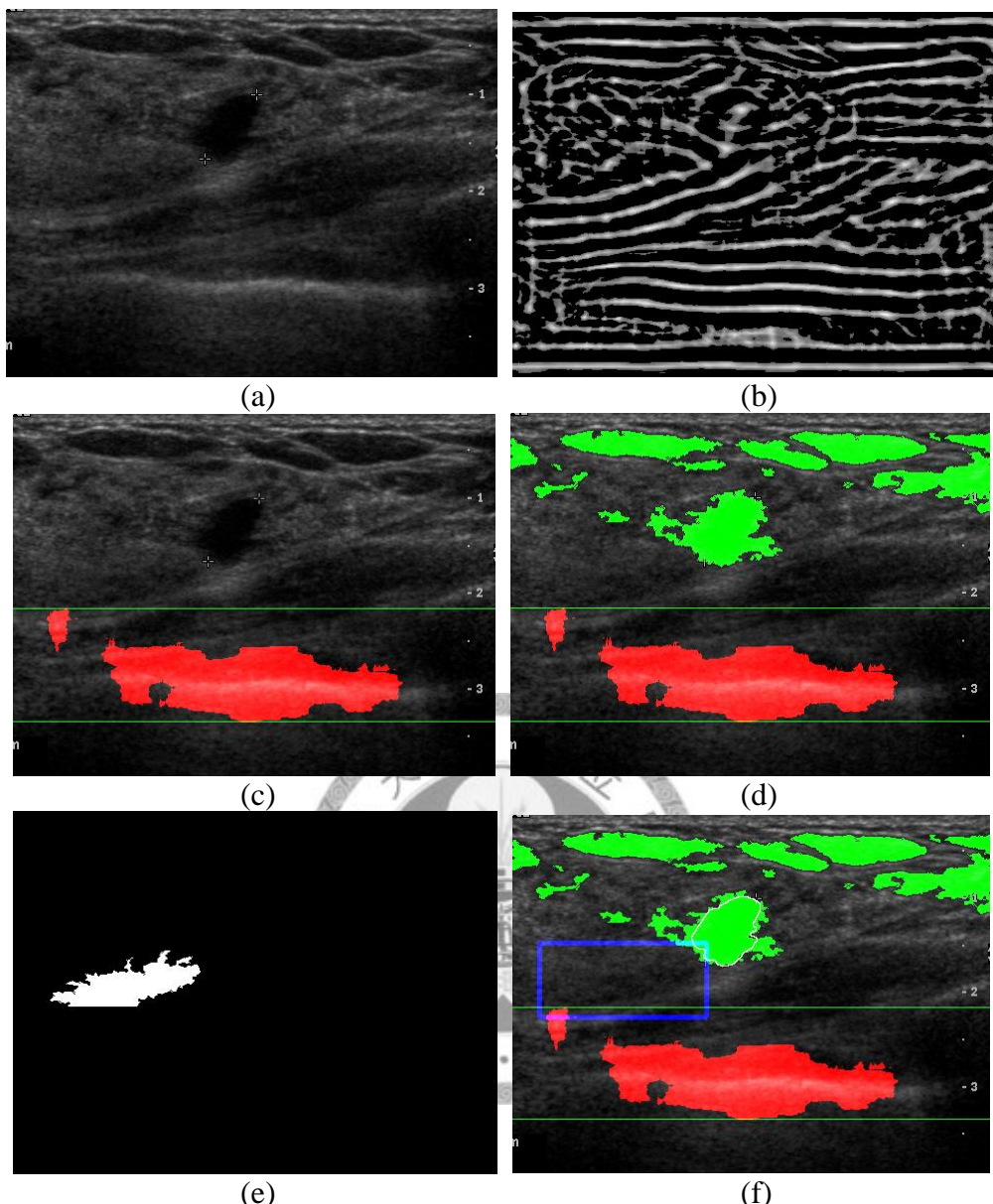


Fig 4.22 An unsuccessful example of malignant lesion, in which the lesion is identified as one part of the fat layer, i.e., a false-negative detection. (a) original image, (b) PS map, (c) the region in-between the two green lines is the detected muscle layer, (d) the green part is the detected fat layer region and (e) the white part in binary image is the detected lesion. (f) the blue rectangle shows the final result by our approach is a false-positive detection and radiologist outline is depicted with white contour.

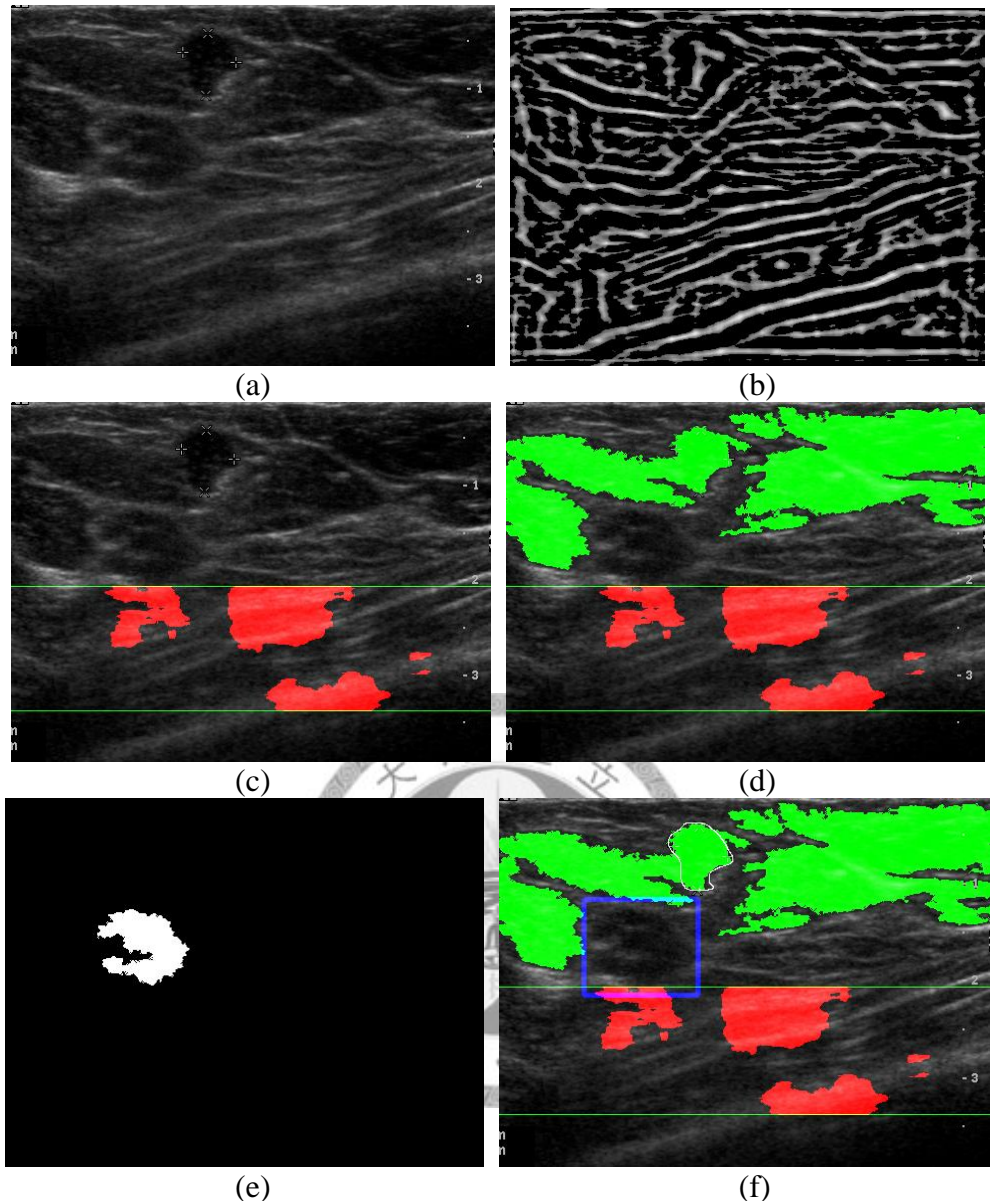


Fig 4.23 An unsuccessful example of malignant lesion, in which the lesion invades the fat layer. The lesion is identified as one part of the fat layer, i.e., a false-negative detection. (a) original image, (b) PS map, (c) the region in-between the two green lines is the detected muscle layer, (d) the green part is the detected fat layer region and (e) the white part in binary image is the detected lesion. (f) the blue rectangle shows the final result by our approach is a false-positive detection and radiologist outline is depicted with white contour.

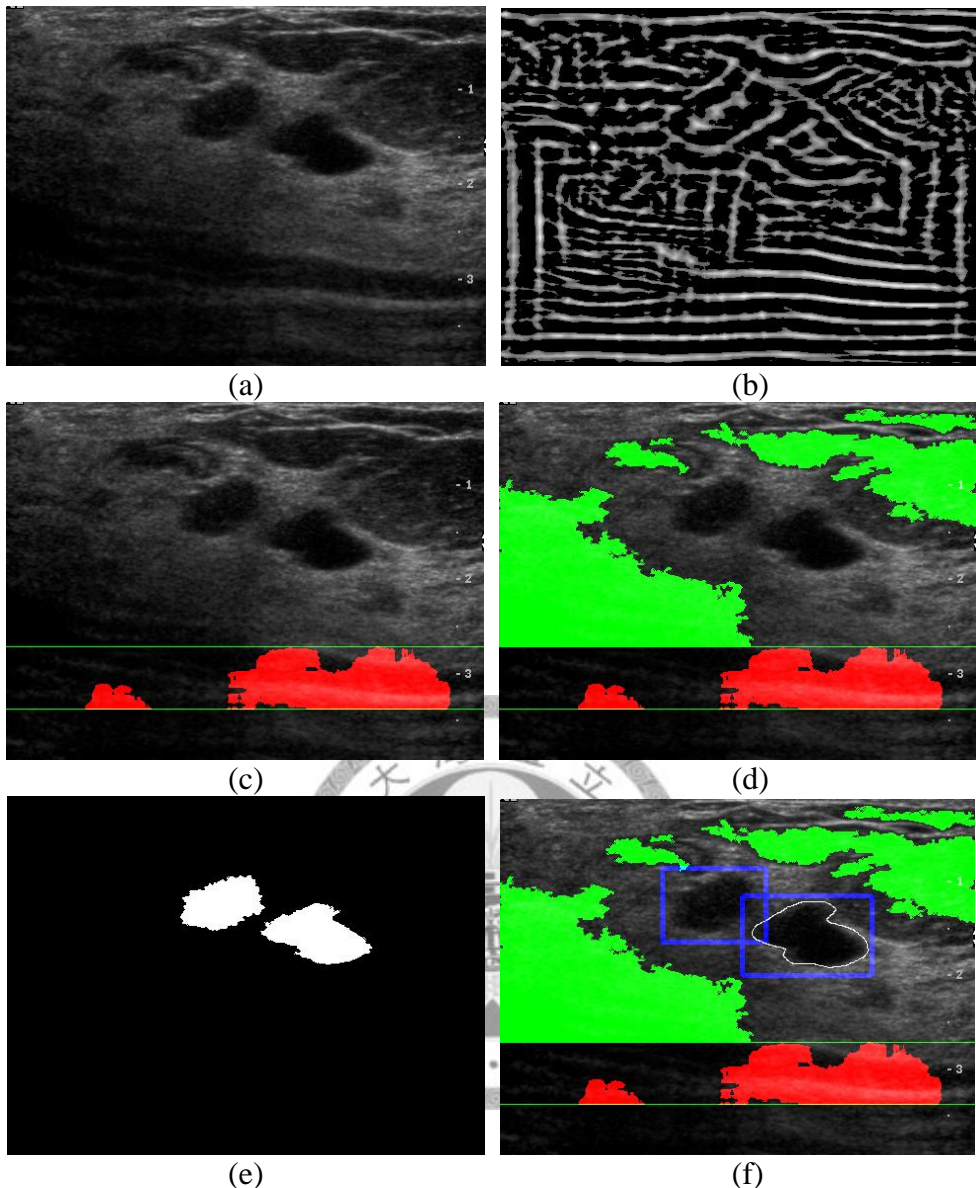


Fig 4.24 An unsuccessful example of malignant lesion, in which the right blue rectangle is a lesion but the left blue rectangle is a false-positive detection. (a) original image, **(b)** PS map, **(c)** the region in-between the two green lines is the detected muscle layer, **(d)** the green part is the detected fat layer region and **(e)** the white part in binary image is the detected lesion. **(f)** the final result of our approach, in which a lesion and a false-positive detection are detected by the blue rectangles and the region enclosed by the white contour is the lesion defined by a radiologist.

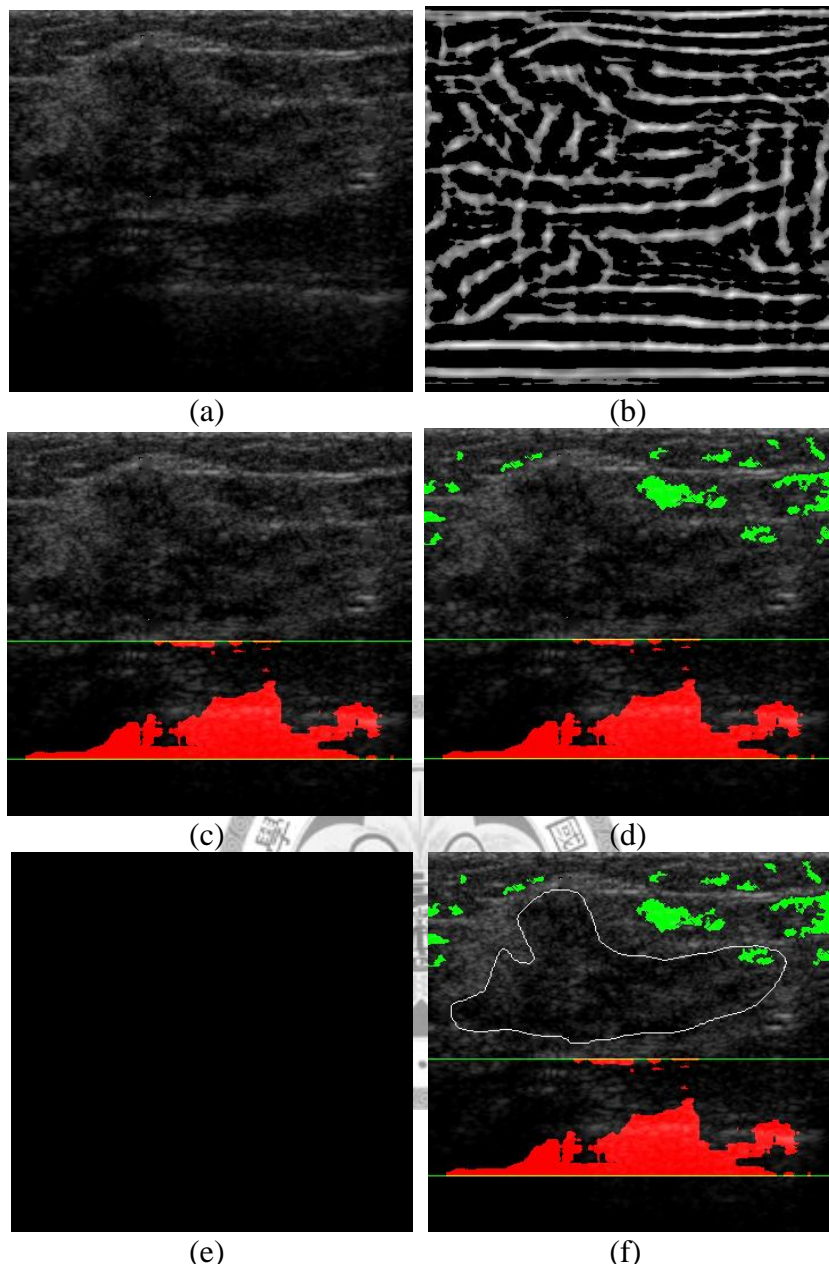


Fig 4.25 An unsuccessful example of malignant lesion, in which no lesion is identified, i.e., a false-negative detection. (a) original image, (b) PS map, (c) the region in-between the two green lines is the detected muscle layer, (d) the green part is the detected fat layer region and (e) the white part in binary image is the detected lesion. (f) the final result of our approach, in which no lesion is detected and the region enclosed by the white contour is the lesion defined by a radiologist.

From these examples which are presented above, it is clear that consider anatomic information to detect lesions will derive precise results. It presents an accuracy table in Table 1.

Table 1 Accuracy of lesion detection estimated by our approach

	Total lesions	TP	FP/image	FN
Number	60	56	6	4
Recognition rate (%)	1	93.33	8.33	6.67

This table shows that lesion detection performance by images based on anatomic information in terms of true-positive (TP), false positive (FP) and false negative (FN) numbers. The number of images used to evaluate performance is 60 images. The TP, FP and FN results show the overall performance of the lesion detection.

There are 60 ultrasound images including 60 lesions used to test this algorithm in this experiment, including cysts, benign and malignant lesions. Most of all could be detected successfully. The results of these experiments prove the accuracy of this proposed approach.

Chapter 5

Conclusion and Discussion

In this thesis the development of the computer-aided detection (CAD) systems to automatically detect lesions via ultrasound images is studied. The processes of the muscle layer, fat layer and lesion detection are all presented in the implementation. It is expected that the proposed method can be used to decrease a false positive rate. In this chapter, we give a conclusion and discuss the feasibility and future works of this algorithm.



It can be difficult to detect lesions on ultrasound image, because of the obscurity of lesions, sonographic artifacts, and operator dependence. However, because most lesions appearing in the breast tissue do not occur in the muscle layer and fat layer; one can get rid of the muscle layer and fat layer in the whole image to increase accuracy of lesion detection. For example, some sonographic artifacts, such as extensive acoustic shadowing on the muscle layer, make lesion detection more difficult. These acoustic shadowed regions can be mistaken as lesions and lead to false-positive detection. In this thesis, a novel automatic CAD system is proposed to identify approximate positions of lesions in whole breast ultrasound images based on the analysis of breast anatomic information; this algorithm can increase accuracy of lesion detection.

This algorithm detects the muscle layer and the fat layer first, and then detects lesions. For muscle layer detection, the basic idea is to fulfill a newly developed texture descriptor which is computed by the Gabor filters, phase symmetry techniques, and estimated entropy of normalized weighting angle distribution of all the patterns to identify the area with rich horizontal strip texture patterns. For fat layer detection, an automatic thresholding approach and topological information are used to label the fat layer in images.

After the fat and muscle layers are determined, suspicious regions in-between these two layers are more likely to be a breast lesion according to the statistic and geometric features, such as a gray level, height-width ratios, region sizes, and location information of lesions.

Although the features we use to detect lesion are few, the result is with high accuracy due to only the part associated with the breast tissue instead of whole image is used for estimation. This method can be applies to cysts, benign lesions, and malignant lesions

because the features are not effected by the type of lesions.

It should be mentioned that the method and evaluation presented here used individual 2D image in a static mode. Ultimately, one can apply our method to developed lesions detection on 3D volume data images or a real-time system in the future.

Recently, the two problems can be considered to be solved in the future. The first is about an exact boundary between the muscle layer and the breast tissue. We present a horizontal line that stands for the upper bound of the muscle layer in each previous example; in fact, the boundary between the muscle layer and the breast tissue is not exactly horizontal. It can be solved by considering the direction of strips in the muscle layer of each image. The second is the case about lesion invading the fat layer. In those cases, the lesions and fat layers are not apt to distinguish by just a gray level and topological information; the clinical knowledge should be considered to solve this problem.

In conclusion, we have presented an automatic detection method based on anatomic structures for breast lesions on ultrasound images. Development of a more effective algorithm to extract lesions in the whole image based on the derived anatomic information is expected. An exact boundary between the muscle layer and the breast tissue instead of a horizontal line for clinical applications or other CAD systems is expected, as well

This method may aid young high-risk females who take breast cancer examination via ultrasound screening. It is also expected to improve the proposed method which can apply to cases as many as possible.

Reference

- [1] Sickles EA. Breast imaging: from 1985 to the present. *Radiology* 2000; 151: 1–16.
- [2] Warner E, Plewes DB, Shumak RS, Catzavelos GC, Di Prospero LS, Yaffe MJ, Ramsay GE, Chart PL, Cole DEC, Taylor GA, Cutrara M, Samuels TH, Murphy JP, Murphy JM, Narod SA. Comparison of breast magnetic resonance imaging, mammography, and ultrasound for surveillance of women at high risk of hereditary breast cancer. *Journal of Clinical Oncology* 2001; 19:3524–3531.
- [3] Buchberger W, DeKoekkoek-Doll P, Springer P, Obrist P, Dunser M. Incidental findings on sonography of the breast: clinical significance and diagnostic workup. *American Journal of Roentgenology* 1999; 173: 921–927.
- [4] Berg WA, Gilbreath PL. Multicentric and multifocal cancer: whole breast US in preoperative evaluation. *Radiology* 2000; 214: 59–66.
- [5] Moon WK, Im JG, Koh YH, Noh DY, Park IA. US of mammographically detected clustered microcalcifications. *Radiology* 2000; 217: 849–854.
- [6] Zonderland HM, Coerkamp EG, Hermans J, van de Vijver MJ, van Voorthuisen AE. Diagnosis of breast cancer: contributions of US as an adjunct to mammography. *Radiology* 1999; 213: 413–422.
- [7] Bassett LW, Israel M, Gold RH, Ysrael C. Usefulness of mammography and sonography in women<35 years old. *Radiography* 1991; 180: 831.
- [8] Kolb TM, Lichy J, Newhouse JH. Occult cancer in women with dense breasts: detection with screening US—diagnostic yield and tumor characteristics. *Radiology* 1998; 207: 191–199.
- [9] Giger ML, Al-Hallaq H, Huo Z, Moran C, Wolverton DE, Chan CW, Zhong W. Computerized analysis of lesions in US images of the breast. *Academic Radiology*

1999; 6 (11):665–674.

- [10] Chiang HK, Tiu CM, Hung GS, Wu SC, Chang TY, Chou YH. Stepwise logistic regression analysis of tumor contour features for breast ultrasound diagnosis. *Ultrasound in Medicine and Biology* 2001; 27 (11):1493–1498.
- [11] Anant Madabhushi, Metaxas DN. Combining low-, high-level and empirical domain knowledge for automated segmentation of ultrasonic breast lesions. *IEEE Transactions on Medical Imaging* 2004; 22(2):155-169.
- [12] Drukker K, Giger ML, Horsch K, Kupinski MA, Vyborny CJ, Mendelson EB. Computerized lesion detection on breast ultrasound. *Medical Physics* 2002; 29: 1438–1446.
- [13] Drukker K, Giger ML, Mendelson EB. Computerized analysis of shadowing on breast ultrasound for improved lesion detection. *Medical Physics* 2003; 30(7): 1833-1842.
- [14] Ikeda Y, Fukuoka D, Hara T, Fujita H, Takada E, Endo T, Morita T. Computer-aided detection system of breast masses on ultrasound images. *Proc. of SPIE* 2006; 6144:1801-1808.
- [15] Chang RF, Chang-Chien KC, Chen HJ, Chen DR, Takada E, Moon WK. Whole breast computer-aided screening using free-hand ultrasound. *IPPR Conference on Computer Vision, Graphics and Image Processing* 2005; 1281:1075-1080.
- [16] Oppenheim AV, Lim JS. The important of phase in signals. *Proc IEEE* 1981; 69(5):529-541.
- [17] Morrone MC, Owens RA. Feature detection from local energy. *Pattern Recognition Letters* 1987; 6:303-313.
- [18] Grau V, Noble AJ. Adaptive multi-scale ultrasound compounding using phase

- information. Proc MICCAI 2005. Lecture Notes in Computer Science 2005; 3749:589-596.
- [19] Kovesi PD. Invariant measures of image features from phase information. PhD thesis, The University of Western Australia 1996.
- [20] Kovesi PD. Symmetry and asymmetry from local phase. Proc Tenth Australian Joint Conference on Artificial Intelligence 1997: 185-190.
- [21] Miguel MP, Noble JA. 2D+T boundary detection in echocardiography. Medical Image Analysis 2000; 4(1):21-30.
- [22] Gerardo SO, Declerck J, Miguel MP, Noble JA. Automatic 3D echocardiographic image analysis. Proc MICCAI 2000. Lecture Notes in Computer Science 2000; 1935: 687-696.
- [23] Daugman JG. Two-dimensional spectral analysis of cortical receptive field profiles. Vision Research 1980; 20:847– 856.
- [24] Young R. The Gaussian derivative theory of spatial vision: analysis of cortical cell receptive field lineweighting profiles. Tech. Rep. GMR-4920 (General Motor Research), Warren, Mich. 1985.
- [25] Malik J, Perona P. Preattentive texture discrimination with early vision Mechanisms mechanisms . Journal of the Optical Society of America 1990; A7: 923–932.
- [26] Jain AK, Farrokhnia F. Unsupervised texture segmentation using Gabor filters. Pattern Recognition 1991; 24(12):1167–1186.
- [27] Wagner RF, Smith SW, Sandrik JM, Lopez H. Statistics of speckle in ultrasound B-scans. IEEE Transactions of Sonics and Ultrasonics 1983; 30(3): 156-163.
- [28] Kovesi PD. Image features from phase congruency. Videre: A Journal of Computer Vision Research 1999: 1(3), 1-26.

- [29] Venkatesh S, Owens R. On the classification of image features. *Pattern Recognition Letters* 1990; 11:339-349.
- [30] Otsu N. A threshold selection method from gray-level histogram. *IEEE Transactions on Systems, Man, and Cybernetics* 1979; 9(1): 62-66.
- [31] Liao PS, Chen TS, Chung PC. A fast algorithm for multilevel thresholding. *Journal of Information Science and Engineering* 2002; 17, 713-727.
- [32] Pollen DA, Ronner SF. Visual cortical neurons as localized spatial frequency filters. *IEEE Transactions on Systems, Man, and Cybernetics* 1983; 13:907–916.

